

# Linearizing the hybridizable discontinuous Galerkin method: A linearly scaling operator

Immo Huismann<sup>\*a,b</sup>, Jörg Stiller<sup>a,b</sup>, and Jochen Fröhlich<sup>a,b</sup>

<sup>a</sup>Institute of Fluid Mechanics, TU Dresden

<sup>b</sup>Center for Advancing Electronics Dresden (cfaed)

July 24, 2020

## Abstract

This paper proposes a matrix-free residual evaluation technique for the hybridizable discontinuous GALERKIN method requiring a number of operations scaling only linearly with the number of degrees of freedom. The method results from application of tensor-product bases on cuboidal Cartesian elements, a specific choice for the penalty parameter, and the fast diagonalization technique. In combination with a linearly scaling, face-wise preconditioner, a linearly scaling iteration time for a conjugate gradient method is attained. This allows for solutions in 1  $\mu$ s per unknown on one CPU core – a number typically associated with low-order methods.

## 1 Introduction

At the front of spatial discretization, high-order methods are the current focus of research, especially continuous and discontinuous GALERKIN spectral-element methods [8, 26, 15]. Where low-order methods use linear shape functions or interpolations, these methods approximate the solution using piece-wise polynomial basis functions. Using an ansatz of order  $p$ , a convergence order of  $p + 1$  can be reached. However, multiple issues arise: First, while the number of degrees of freedom in three dimensions scales with  $n_{\text{DOF}} \approx p^3 n_e$ , where  $n_e$  represents the number of elements, most operator evaluations scale with  $\mathcal{O}(p^4 n_e) = \mathcal{O}(p n_{\text{DOF}})$  when exploiting tensor-product bases, i.e. super-linearly with the number of degrees of freedom [8]. Second, the time step restriction from convection terms scales with  $1/p^2$  and even with  $1/p^4$  for diffusion [26]. While fully explicit approaches are often preferred for compressible flows [16], the incompressible case requires implicit treatment of diffusion and pressure to avoid crippling time stepping restrictions. The occurring elliptic equations often take the form  $\lambda u - \Delta u = f$  for a non-negative  $\lambda$  [27, 12]. The runtime spent in the corresponding elliptic solvers can amount to 90 % of the cost [9]. Therefore, efficient solution of these equations is of central importance for a well-performing high-order flow solver. The optimum would be a linearly scaling solver which, therefore, is the target.

This paper considers the discontinuous GALERKIN method (DG) for discretization on Cartesian grids. While DG itself was first developed in conjunction with time-stepping for convection problems [25], it was quickly adapted to spatial discretization [7], generating

---

\*Corresponding author: Immo.Huismann@tu-dresden.de

a plethora of different formulations ranging from interior penalty to local discontinuous ones [1]. Here, the local discontinuous GALERKIN method (LDG) [4] is utilized. The method allows for hybridization, i.e. using only the fluxes for the solution variable instead of the whole equation system. This leads to the hybridized local discontinuous Galerkin method (LDG-H), which reduces the number of algebraic unknowns from  $\mathcal{O}(p^3)$  to  $\mathcal{O}(p^2)$  [28, 38, 6]. While every suboperator of the resulting equation system can be expressed in matrix-free form [29], the operator itself still scales with  $\mathcal{O}(pn_{\text{DOF}})$ . For a solver to scale linearly with the number of unknowns when increasing the polynomial degree, a linearly scaling operator is mandatory. While these linearly scaling operators are available for the continuous discretization [22, 24, 17], they have so far only been postulated for the discontinuous one [29], and, to the knowledge of the authors, no implementation thereof exists.

In previous work [22, 24], the present authors have considered a continuous spectral-element discretization, developing a linearly scaling operator which, in conjunction with multigrid techniques, allows for a linearly scaling elliptic solver. The resulting runtime scales with  $\mathcal{O}(n_{\text{DOF}})$  independent of the polynomial degree. The goal of this paper is to transfer these methods for the operator evaluation from the continuous discretization to the discontinuous one, i.e. to a hybridizable discontinuous GALERKIN operator. It will be shown that, indeed, a linearly scaling operation account is achieved, which can be extended to a solver with an iteration time that scales linearly with the number of degrees of freedom and a runtime that scales linearly with them when increasing  $p$ . While the methods are presented here using LDG-H, they can be similarly applied to the hybridizable interior penalty method described in [10].

The structure of the paper is as follows: First, the discretization with LDG and LDG-H is considered in Section 2, and a linearly scaling operator derived for the one-dimensional case. Then, the discretization and required operators are expanded to three dimensions in Section 3. Thereafter in Section 4, sum and product factorization are applied to the operator, linearizing its operation count and validating the linear scaling with runtime tests. Lastly, Section 5 considers solvers with linearly scaling iteration time.

## 2 The Hybridized Discontinuous Galerkin method in one dimension

### 2.1 Local Discontinuous Galerkin discretization

This paper considers the hybridized discontinuous GALERKIN method, introduced, for instance, in [28, 38, 29], with a focus on the tensor-product operators. To establish nomenclature and allow for a clearer understanding of the derivation of the linear solver, this section reiterates the basics thereof. More expansive introductions to DG as well as HDG can be found in [15, 6, 5].

The considered elliptic equation reads

$$\lambda u - \Delta u = f \quad \text{in } \Omega \quad , \quad (1a)$$

where  $\Omega$  denotes the computational domain and, for each point  $\vec{x} \in \Omega$ ,  $u(\vec{x})$  the solution variable and  $f(\vec{x})$  the right-hand side. Furthermore,  $\lambda$  constitutes a non-negative parameter. This equation is supplemented by boundary conditions

$$u = g_{\text{D}} \quad \text{on } \partial\Omega_{\text{D}} \quad (1b)$$

$$\vec{n} \cdot \nabla u = g_{\text{N}} \quad \text{on } \partial\Omega_{\text{N}} \quad , \quad (1c)$$

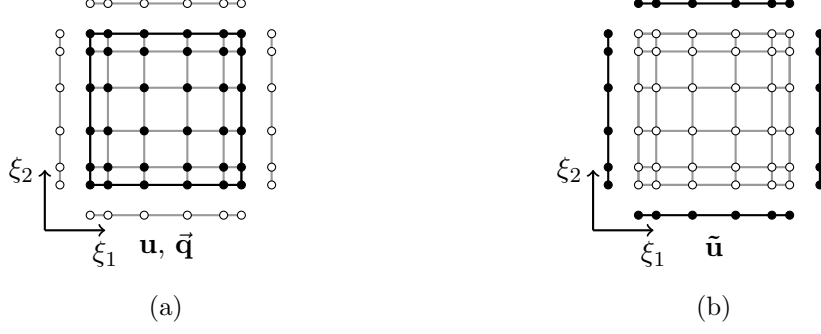


Figure 1: Arrangement of variables for high order methods. Filled nodes indicate locations of the solution variables, whereas empty ones are only used in intermediate steps. (a): In local discontinuous DG formulations, the solution variable  $u$  and auxiliary variable  $\vec{q}$  are utilized, with the flux only receiving an intermediate role. (b): In HDG, only the flux  $\tilde{u}$  of the solution variable  $u$  remains.

with  $\partial\Omega_D$  denoting a DIRICHLET boundary,  $\partial\Omega_N$  a NEUMANN boundary, and  $g_N$  and  $g_D$  the corresponding boundary values. The introduction of an auxiliary variable  $\vec{q}$  allows to rewrite (1a) in the so-called flux form

$$\lambda u - \nabla \cdot \vec{q} = f \quad (2a)$$

$$\vec{q} = \nabla u \quad , \quad (2b)$$

with boundary conditions

$$u = g_D \quad \text{on } \partial\Omega_D \quad (2c)$$

$$\vec{n} \cdot \vec{q} = g_N \quad \text{on } \partial\Omega_N \quad . \quad (2d)$$

Using the test functions  $v, \vec{w}, \mu$ , equations (2a), (2b), and (2d) can be cast into the weak form

$$\int_{\vec{x} \in \Omega} \lambda u v \, d\vec{x} + \int_{\vec{x} \in \Omega} \nabla v \cdot \vec{q} \, d\vec{x} = \int_{\vec{x} \in \Omega} v f \, d\vec{x} + \int_{\vec{x} \in \partial\Omega} v \vec{n} \cdot \vec{q} \, d\vec{x} \quad (3a)$$

$$\int_{\vec{x} \in \Omega} \vec{w} \cdot \vec{q} \, d\vec{x} = - \int_{\vec{x} \in \Omega} \nabla \cdot \vec{w} u \, d\vec{x} + \int_{\vec{x} \in \partial\Omega} \vec{w} \cdot \vec{n} \tilde{u} \, d\vec{x} \quad (3b)$$

$$\int_{\vec{x} \in \partial\Omega} \mu \vec{q} \cdot \vec{n} \, d\vec{x} = \int_{\vec{x} \in \partial\Omega_N} \mu g_N \, d\vec{x} \quad , \quad (3c)$$

where the fluxes  $\tilde{u}$  and  $\vec{q}$  approximate the boundary values of  $u$  and  $\vec{q}$ .

When discretizing the weighted flux form (3b), the solution variables are  $u$  and  $\vec{q}$ , whereas the fluxes only serve as dependent variable used to couple the elements, as sketched in Figure 1. The main idea of hybridization lies in eliminating  $u$ ,  $\vec{q}$ , and  $\vec{q}$  from system (3) such that only the flux  $\tilde{u}$  remains as solution variable. This leads to the condition that, after decomposing the domain  $\Omega$  into  $n_e$  elements  $\Omega_e$ , the solution for  $u$  and  $\vec{q}$  in each element should solely depend on the boundary flux  $\tilde{u}$  on each element, which limits the choice of the fluxes. These are chosen in accordance with [5] here to be

$$\tilde{u} = \frac{\tau^+}{\tau^+ + \tau^-} u^+ + \frac{\tau^-}{\tau^+ + \tau^-} u^- - \frac{1}{\tau^+ + \tau^-} (\vec{q}^+ \cdot \vec{n}^+ + \vec{q}^- \cdot \vec{n}^-) \quad (4a)$$

$$\vec{q} = \frac{\tau^+}{\tau^+ + \tau^-} \vec{q}^+ + \frac{\tau^-}{\tau^+ + \tau^-} \vec{q}^- - \frac{\tau^+ \tau^-}{\tau^+ + \tau^-} (u^+ \cdot \vec{n}^+ + u^- \cdot \vec{n}^-) \quad , \quad (4b)$$

where the superscripts  $+$  and  $-$  denote traces from the two adjoining elements on a boundary and  $\tau^+$  and  $\tau^-$  the corresponding penalty parameters. For each element, the flux  $\vec{q}$  equates to

$$\vec{q}(\vec{x}) = \vec{q}(\vec{x}) - \tau_e \vec{n}(\vec{x}) (u(\vec{x}) - \tilde{u}(\vec{x})) \quad \forall \vec{x} \in \partial\Omega_e \quad , \quad (5)$$

where  $\tau_e$  is the penalty parameter.

Inserting and (5) into (3) leads to the element equations. This process simplifies (3a) to

$$\int_{\vec{x} \in \Omega_e} \lambda uv \, d\vec{x} + \int_{\vec{x} \in \partial\Omega_e} \tau_e v u \, d\vec{x} - \int_{\vec{x} \in \Omega_e} v \nabla \cdot \vec{q} \, d\vec{x} = \int_{\vec{x} \in \Omega_e} v f \, d\vec{x} + \int_{\vec{x} \in \partial\Omega_e} \tau_e v \tilde{u} \, d\vec{x} \quad , \quad (6a)$$

again dropping the dependence on  $\vec{x}$  for sake of readability. Here, the third term was integrated by parts a second time to gain a symmetric equation system. Moreover, (3b) becomes

$$\int_{\vec{x} \in \Omega_e} \vec{w} \cdot \vec{q} \, d\vec{x} = - \int_{\vec{x} \in \Omega_e} \nabla \cdot \vec{w} u \, d\vec{x} + \int_{\vec{x} \in \partial\Omega_e} \vec{w} \cdot \vec{n} \tilde{u} \, d\vec{x} \quad (6b)$$

and, lastly, inserting (5) into (3c) yields

$$\sum_e \left[ \int_{\vec{x} \in \partial\Omega_e} \mu \vec{q} \cdot \vec{n} \, d\vec{x} + \int_{\vec{x} \in \partial\Omega_e} \mu \tilde{u} \, d\vec{x} - \int_{\vec{x} \in \partial\Omega_e} \tau_e \mu u \, d\vec{x} \right] = \int_{\vec{x} \in \partial\Omega_N} \mu g_N \, d\vec{x} \quad . \quad (6c)$$

## 2.2 HDG operators in one dimension

In this section, a HDG operator is derived in one dimension. Here,  $\vec{q}$  has only got one component,  $q$ . A set of polynomial basis functions  $\{\varphi_i(\xi)\}_{i=0}^p$  is introduced for  $u$  and  $q$  on the standard element  $\Omega^S = [-1, 1]$  and mapped to each element. Moreover, in each element  $\Omega_e$   $\tilde{u}$  has two values, each of them being one on their respective boundary while vanishing on the other, such that two basis functions  $\phi_i : \partial\Omega^S \rightarrow \{0, 1\}$ ,  $i \in \{1, 2\}$ , describe the fluxes  $\tilde{u}$  on the left and right boundary with  $\phi_1(-1) = 1, \phi_1(1) = 0$  and  $\phi_2(-1) = 0, \phi_2(1) = 1$ . Furthermore, the penalty parameter occurring in (5) and (6a) is chosen as

$$\tau_e = \frac{2}{h_e} \hat{\tau} \quad , \quad (7)$$

where  $h_e$  denotes the width of  $\Omega_e$ . Inserting the basis functions and penalty parameter into (6) leads to the following standard matrices and element matrices

$$M_{ij} = \int_{\xi \in \Omega^S} \varphi_i \varphi_j \, d\xi \quad \mathbf{M}_e = \frac{h_e}{2} \mathbf{M} \quad (8a)$$

$$D_{ij} = \int_{\xi \in \Omega^S} \varphi_i \partial_\xi \varphi_j \, d\xi \quad \mathbf{D}_e = \mathbf{D} \quad (8b)$$

$$E_{ij} = +\hat{\tau} [(\varphi_i \varphi_j)(-1) + (\varphi_i \varphi_j)(+1)] \quad \mathbf{E}_e = \frac{2}{h_e} \mathbf{E} \quad (8c)$$

$$G_{ij} = +\hat{\tau} [(\phi_i \phi_j)(-1) + (\phi_i \phi_j)(+1)] \quad \mathbf{G}_e = \frac{2}{h_e} \mathbf{G} \quad (8d)$$

$$B_{ij} = -\hat{\tau} [(\varphi_i \phi_j)(-1) + (\varphi_i \phi_j)(+1)] \quad \mathbf{B}_e = \frac{2}{h_e} \mathbf{B} \quad (8e)$$

$$C_{ij} = [(\varphi_i \phi_j \vec{n})(-1) + (\varphi_i \phi_j \vec{n})(+1)] \quad \mathbf{C}_e = \mathbf{C} \quad . \quad (8f)$$

Here,  $\mathbf{M}$  denotes the standard element mass matrix,  $\mathbf{D}$  the standard element differentiation matrix, and  $\mathbf{L}$  the stiffness matrix. Furthermore, the stiffness matrix results from

$$\mathbf{L} = \mathbf{E} + \mathbf{D}\mathbf{M}^{-1}\mathbf{D}^T \quad \mathbf{L}_e = \frac{2}{h_e}\mathbf{L} \quad . \quad (8g)$$

It is to be noted that the stiffness matrix  $\mathbf{L}$  differs from the one in the continuous case: The differentiation matrices are transposed and a further penalty term is present.

With the element matrices, the equation system (6) takes the form

$$\sum_e \mathbf{Q}_e^T \begin{pmatrix} \lambda\mathbf{M}_e + \mathbf{E}_e & -\mathbf{D}_e & \mathbf{B}_e \\ -\mathbf{D}_e^T & -\mathbf{M}_e & \mathbf{C}_e \\ \mathbf{B}_e^T & \mathbf{C}_e^T & \mathbf{G}_e \end{pmatrix} \begin{pmatrix} \mathbf{u}_e \\ \mathbf{q}_e \\ \tilde{\mathbf{u}}_e \end{pmatrix} = \sum_e \mathbf{Q}_e^T \begin{pmatrix} \mathbf{M}_e \mathbf{f}_e \\ \mathbf{0} \\ \mathbf{g}_{N,e} \end{pmatrix} \quad , \quad (9)$$

where  $\mathbf{Q}_e^T$  gathers the contributions from several elements for the global degrees of freedom and boldface denotes the coefficient vectors, e.g.  $\mathbf{u}_e$  for the coefficients on the element for  $u$ . As the solution and the auxiliary variable are discontinuous, the element coefficients are the global degrees of freedom. Therefore, the first two lines remain local to the element. The last line couples the elements, with the right-hand side  $\mathbf{g}_{N,e}$  denoting either the NEUMANN boundary condition, or zero. Eliminating  $\mathbf{u}_e$  and  $\mathbf{q}_e$  from (9) leads to a global equation system of the form

$$\mathbf{K}\tilde{\mathbf{u}} = \mathbf{F}^{\text{HDG}} \quad (10)$$

which can be rewritten as

$$\sum_e \tilde{\mathbf{Q}}_e^T \mathbf{K}_e \underbrace{\tilde{\mathbf{Q}}_e}_{\tilde{\mathbf{u}}_e} \tilde{\mathbf{u}} = \sum_e \tilde{\mathbf{Q}}_e^T \mathbf{F}_e^{\text{HDG}} \quad (11)$$

where  $\mathbf{K}_e$  denotes the element operator,  $\mathbf{F}^{\text{HDG}}$  the right-hand side and  $\tilde{\mathbf{Q}}_e$  the matrix mapping global flux degrees of freedom to element-local ones. The element operators  $\mathbf{K}_e$  result via SCHUR complement of (9)

$$\mathbf{K}_e = \mathbf{G}_e - \underbrace{\begin{pmatrix} \mathbf{B}_e \\ \mathbf{C}_e \end{pmatrix}^T}_{\mathbf{R}_e^T} \mathbf{A}_e^{-1} \underbrace{\begin{pmatrix} \mathbf{B}_e \\ \mathbf{C}_e \end{pmatrix}}_{\mathbf{R}_e} \quad , \quad (12)$$

where  $\mathbf{A}_e$  denotes the coupling between  $\mathbf{u}$  and  $\mathbf{q}$  such that

$$\mathbf{A}_e = \begin{pmatrix} \lambda\mathbf{M}_e + \mathbf{E}_e & -\mathbf{D}_e \\ -\mathbf{D}_e^T & -\mathbf{M}_e \end{pmatrix} \quad . \quad (13)$$

The above matrix can be explicitly inverted, e.g. via SCHUR complement, leading to

$$\mathbf{A}_e^{-1} = \underbrace{\begin{pmatrix} \mathbf{I} \\ -\mathbf{M}_e^{-T}\mathbf{D}_e^T \end{pmatrix}}_{\mathbf{P}_e^T} \underbrace{(\lambda\mathbf{M}_e + \mathbf{E}_e + \mathbf{D}_e\mathbf{M}_e^{-1}\mathbf{D}_e^T)^{-1}}_{\mathbf{Z}_e} \underbrace{(\mathbf{I} \quad -\mathbf{D}_e\mathbf{M}_e^{-1})}_{\mathbf{P}_e} - \begin{pmatrix} \mathbf{0} & \mathbf{0} \\ \mathbf{0} & \mathbf{M}_e^{-1} \end{pmatrix} \quad . \quad (14)$$

The application of the element operator  $\mathbf{K}_e$  contains four steps: First, the diagonal matrix  $\mathbf{G}_e$  integrates on the faces. Then,  $\mathbf{P}_e$  computes the residual induced by the fluxes  $\tilde{\mathbf{u}}_e$  in the inner element for  $\mathbf{u}_e$  and  $\mathbf{q}_e$ , and from these the resulting  $\mathbf{u}_e$  and  $\mathbf{q}_e$  via  $\mathbf{A}_e^{-1}$ . Lastly, applying  $\mathbf{P}_e^T$  computes the effects of the solution inferred into the element onto the flux  $\tilde{\mathbf{u}}_e$ .

### 2.3 Linearly scaling, matrix-free HDG operator evaluation

For evaluation of the HDG element operator, fast application of  $\mathbf{A}_e^{-1}$  is key. The matrix  $\mathbf{Z}_e$  is the main obstacle, as it is a dense, of size  $(p+1) \times (p+1)$ , and differs from element to element. The specific choice of  $\tau_e$  in (7) allows to describe  $\mathbf{Z}_e$  with the same two matrices in every element:

$$\mathbf{Z}_e^{-1} = \lambda \mathbf{M}_e + \mathbf{E}_e + \mathbf{D}_e \mathbf{M}_e^{-1} \mathbf{D}_e^T \quad (15)$$

$$\mathbf{L}_e = \mathbf{E}_e + \mathbf{D}_e \mathbf{M}_e^{-1} \mathbf{D}_e^T \quad (16)$$

$$\Rightarrow \mathbf{Z}_e = (\lambda \mathbf{M}_e + \mathbf{L}_e)^{-1} = \left( \frac{\lambda h_e}{2} \mathbf{M} + \frac{2}{h_e} \mathbf{L} \right)^{-1} . \quad (17)$$

This allows for a generalized eigenvalue decomposition

$$\mathbf{S}^T \mathbf{M} \mathbf{S} = \mathbf{I} \quad (18a)$$

$$\mathbf{S}^T \mathbf{L} \mathbf{S} = \mathbf{\Lambda} , \quad (18b)$$

where  $\mathbf{S}$  is a non-orthogonal transformation matrix, and  $\mathbf{\Lambda}$  a diagonal matrix containing the eigenvalues. Using these, the inverse computes to

$$\mathbf{Z}_e = \mathbf{S} \mathbf{D}_{\mathbf{Z}_e}^{-1} \mathbf{S}^T , \quad (19)$$

where

$$\mathbf{D}_{\mathbf{Z}_e} = \frac{\lambda h_e}{2} \mathbf{I} + \frac{2}{h_e} \mathbf{\Lambda} . \quad (20)$$

With this representation, the inverse of  $\mathbf{A}_e$  can be modified with respect to (14), now reading

$$\mathbf{A}_e^{-1} = \mathbf{P}_e^T \mathbf{S} \mathbf{D}_{\mathbf{Z}_e}^{-1} \mathbf{S}^T \mathbf{P}_e - \begin{pmatrix} \mathbf{0} & \mathbf{0} \\ \mathbf{0} & \mathbf{M}_e^{-1} \end{pmatrix} . \quad (21)$$

Inserting (21) into the element operator  $\mathbf{K}_e$  leads to

$$\mathbf{K}_e = \mathbf{G}_e - \underbrace{\begin{pmatrix} \mathbf{B}_e^T & \mathbf{C}_e^T \end{pmatrix}}_{\mathbf{R}_e^T} \left[ \mathbf{P}_e^T \mathbf{S} \mathbf{D}_{\mathbf{Z}_e}^{-1} \mathbf{S}^T \mathbf{P}_e - \begin{pmatrix} \mathbf{0} & \mathbf{0} \\ \mathbf{0} & \mathbf{M}_e^{-1} \end{pmatrix} \right] \underbrace{\begin{pmatrix} \mathbf{B}_e \\ \mathbf{C}_e \end{pmatrix}}_{\mathbf{R}_e} , \quad (22)$$

such that further evaluation yields

$$\mathbf{K}_e = \mathbf{G}_e + \mathbf{C}_e^T \mathbf{M}_e^{-1} \mathbf{C}_e - \mathbf{R}_e^T \mathbf{P}_e^T \mathbf{S} \mathbf{D}_{\mathbf{Z}_e}^{-1} \mathbf{S}^T \mathbf{P}_e \mathbf{R}_e \quad (23)$$

or, equivalently,

$$\mathbf{K}_e = \frac{2}{h_e} \mathbf{G} + \frac{2}{h_e} \mathbf{C}^T \mathbf{M}^{-1} \mathbf{C} - \frac{2}{h_e} \mathbf{R}^T \mathbf{P}^T \mathbf{S} \mathbf{D}_{\mathbf{Z}_e}^{-1} \mathbf{S}^T \mathbf{P} \mathbf{R} \frac{2}{h_e} . \quad (24)$$

The last form consists of three terms. Application of the first two just requires one  $2 \times 2$  matrix product, whereas the latter consists of using a row matrix to generate the right-hand side for  $\mathbf{u}$ , using the inverse eigenvalues, and then a reduction back to the fluxes.

The ultimate goal lies in a linearly scaling, matrix-free HDG operator in three dimensions. To this end, the one-dimensional case of (24) serves as a prototype. To attain a

---

**Algorithm 1** Computation of the effect of the HDG operator on a per-element basis, where  $d_{1,e} = h_e/2$  denotes the metric coefficient.

---

```

function HDG_OP_1D( $\tilde{\mathbf{u}}$ )
  for  $e = 1, n_e$  do
     $\mathbf{F}_E \leftarrow d_{1,e} \mathbf{B}_S \tilde{\mathbf{u}}_e$ 
     $\mathbf{u}_E \leftarrow \mathbf{D}_{\mathbf{z}_e}^{-1} \mathbf{F}_E$ 
     $\tilde{\mathbf{r}}_e \leftarrow d_{1,e} (\mathbf{G} + \mathbf{C}^T \mathbf{M}^{-1} \mathbf{C}) \tilde{\mathbf{u}}_e - d_{1,e} \mathbf{B}_S^T \mathbf{u}_E$ 
  end for
  return  $\tilde{\mathbf{r}}$ 
end function

```

---

linearly scaling algorithm for the residual evaluation, the row matrix mapping into the element eigenspace requires an explicit representation:

$$\mathbf{B}_S = \mathbf{S}^T \mathbf{P} \mathbf{R} = \mathbf{S}^T (\mathbf{I} \quad -\mathbf{D} \mathbf{M}^{-1}) \begin{pmatrix} \mathbf{B} \\ \mathbf{C} \end{pmatrix} = \mathbf{S}^T \mathbf{B} - \mathbf{S}^T \mathbf{D} \mathbf{M}^{-1} \mathbf{C} \quad . \quad (25)$$

Using this mapping, the element-wise HDG residual can be evaluated via Algorithm 1, which requires  $\mathcal{O}(pn_e)$  operations. First, the operator computes the residual  $\mathbf{F}_E$  in the element eigenspace by applying  $\mathbf{B}_S$  to the fluxes and then computes a solution  $\mathbf{u}_E$  in the eigenspace by applying the inverse eigenvalues  $\mathbf{D}_{\mathbf{z}_e}^{-1}$ . Lastly, the effect of  $\mathbf{u}_E$  onto  $\tilde{\mathbf{u}}_e$  results by applying  $\mathbf{B}_S^T$  on the solution  $\mathbf{u}_E$  and the diagonal term. The three operators of mapping into the element eigenspace, applying the inverse eigenvalues, and, lastly, mapping back generate an operation count  $5(p+1)$ , whereas the application of  $(\mathbf{G} + \mathbf{C}^T \mathbf{M}^{-1} \mathbf{C})$  requires 8 operations per element. Therefore, Algorithm 1 constitutes a linearly scaling, matrix-free residual evaluation technique, albeit only for the one-dimensional case.

### 3 The HDG element operator in three dimensions

#### 3.1 Tensor-product matrices

In this section, a tensor-product basis is considered. This provides further structure to the operators and leads to tensor-product matrices, as introduced in [30, 8]. For  $\mathbf{A}, \mathbf{B} \in \mathbb{R}^{n,n}$ , the tensor product  $\mathbf{B} \otimes \mathbf{A} \in \mathbb{R}^{n^2, n^2}$  is defined as

$$\mathbf{B} \otimes \mathbf{A} = \begin{pmatrix} \mathbf{A}B_{11} & \mathbf{A}B_{12} & \dots & \mathbf{A}B_{1n} \\ \mathbf{A}B_{21} & \mathbf{A}B_{22} & \dots & \mathbf{A}B_{2n} \\ \vdots & \vdots & \ddots & \vdots \\ \mathbf{A}B_{n1} & \mathbf{A}B_{n2} & \dots & \mathbf{A}B_{nn} \end{pmatrix} \quad . \quad (26)$$

Where the application of the matrix  $\mathbf{B} \otimes \mathbf{A}$  as a whole to a vector  $\mathbf{u} \in \mathbb{R}^{n^2}$  incurs  $2n^4$  operations, the tensor-product can be applied by, first, using matrix  $\mathbf{A}$  in the first direction and then  $\mathbf{B}$  in the second. As only two one-dimensional matrix products are involved,  $2 \cdot 2n^{2+1}$  operations occur. Furthermore, the following properties directly result from (26):

$$(\mathbf{B} \otimes \mathbf{A})^T = \mathbf{B}^T \otimes \mathbf{A}^T \quad (27a)$$

$$(\mathbf{B} \otimes \mathbf{A})(\mathbf{D} \otimes \mathbf{C}) = (\mathbf{B}\mathbf{D}) \otimes (\mathbf{A}\mathbf{C}) \quad . \quad (27b)$$

The extension to three dimensions is straight-forward via  $\mathbf{C} \otimes (\mathbf{B} \otimes \mathbf{A})$ , retaining the properties and raising the operation count to  $3 \cdot 2n^{3+1}$ , as is the extension to non-square matrices.

### 3.2 LDG operator structure in three dimensions

Algorithm 1 provides a linearly scaling residual evaluation for HDG in one dimension. In this section it will be extended to three dimensions by inferring a tensor-product structure into the three-dimensional HDG operator.

When expanding the LDG discretization to three dimensions, the vector  $\vec{\mathbf{q}}$  has three components,  $\mathbf{q}_1$ ,  $\mathbf{q}_2$ , and  $\mathbf{q}_3$ . Here, only Cartesian cuboidal elements with tensor-product bases are considered, which allows for a separation of the dimensions: The flux vector  $\tilde{\mathbf{u}}$  can be separated into three parts,  $\tilde{\mathbf{u}}_1$ ,  $\tilde{\mathbf{u}}_2$ , and  $\tilde{\mathbf{u}}_3$ , each residing on the faces in the respective direction. Moreover, the axis-aligned grid removes inter-dependencies in the derivatives: In each direction  $x_i$ , the auxiliary variable  $\mathbf{q}_i$  solely depends on  $\mathbf{u}$  and the corresponding flux  $\tilde{\mathbf{u}}_i$ . This yields the element equation system

$$\sum_e \mathbf{Q}_e^T \begin{pmatrix} \lambda \mathbf{M}_e + \mathbf{E}_e & -\mathbf{D}_{1,e} & -\mathbf{D}_{2,e} & -\mathbf{D}_{3,e} & \mathbf{B}_{1,e} & \mathbf{B}_{2,e} & \mathbf{B}_{3,e} \\ -\mathbf{D}_{1,e}^T & -\mathbf{M}_e & \mathbf{0} & \mathbf{0} & \mathbf{C}_{1,e} & \mathbf{0} & \mathbf{0} \\ -\mathbf{D}_{2,e}^T & \mathbf{0} & -\mathbf{M}_e & \mathbf{0} & \mathbf{0} & \mathbf{C}_{2,e} & \mathbf{0} \\ -\mathbf{D}_{3,e}^T & \mathbf{0} & \mathbf{0} & -\mathbf{M}_e & \mathbf{0} & \mathbf{0} & \mathbf{C}_{3,e} \\ \mathbf{B}_{1,e}^T & \mathbf{C}_{1,e}^T & \mathbf{0} & \mathbf{0} & \mathbf{G}_{1,e} & \mathbf{0} & \mathbf{0} \\ \mathbf{B}_{2,e}^T & \mathbf{0} & \mathbf{C}_{2,e}^T & \mathbf{0} & \mathbf{0} & \mathbf{G}_{2,e} & \mathbf{0} \\ \mathbf{B}_{3,e}^T & \mathbf{0} & \mathbf{0} & \mathbf{C}_{3,e}^T & \mathbf{0} & \mathbf{0} & \mathbf{G}_{3,e} \end{pmatrix} \begin{pmatrix} \mathbf{u}_e \\ \mathbf{q}_{1,e} \\ \mathbf{q}_{2,e} \\ \mathbf{q}_{3,e} \\ \tilde{\mathbf{u}}_{1,e} \\ \tilde{\mathbf{u}}_{2,e} \\ \tilde{\mathbf{u}}_{3,e} \end{pmatrix} = \sum_e \mathbf{Q}_e^T \begin{pmatrix} \mathbf{M}_e \mathbf{f}_e \\ \mathbf{0} \\ \mathbf{0} \\ \mathbf{0} \\ \mathbf{g}_{1,N,e} \\ \mathbf{g}_{2,N,e} \\ \mathbf{g}_{3,N,e} \end{pmatrix}, \quad (28)$$

where the subscript  $e$  denotes the element operator for the three-dimensional element, and the subscripts 1, 2, and 3 indicate the respective direction for the operation. For application of the matrix in (28), similar operators as in the one-dimensional case are required. Let  $h_{i,e}$  denote the element width of  $\Omega_e$  in direction  $x_i$ , which leads to the metric factors

$$(d_{0,e} \ d_{1,e} \ d_{2,e} \ d_{3,e}) = \frac{h_{1,e} h_{2,e} h_{3,e}}{8} \left( 1 \quad \left(\frac{2}{h_{1,e}}\right)^2 \quad \left(\frac{2}{h_{2,e}}\right)^2 \quad \left(\frac{2}{h_{3,e}}\right)^2 \right). \quad (29)$$

As in the one-dimensional case, the penalty parameter is chosen as

$$\tau_{i,e} = \frac{2}{h_{i,e}} \hat{\tau}, \quad (30)$$

which allows for factorization further down the line. A three-dimensional tensor-product base  $\{\varphi_i(\xi_1) \varphi_j(\xi_2) \varphi_k(\xi_3)\}_{i,j,k=0}^p$  on the standard element  $\Omega^S = [-1, 1]^3$  is utilized, where  $\vec{\xi}$  denotes the standard coordinates in three dimensions. Furthermore, the basis for the fluxes results from the tensor-product base at the element boundaries, e.g.  $\xi_1 = -1$ . Figure 1 depicts the two-dimensional case. Using this notation, the insertion of the tensor-product base into (6) leads to the tensor-product matrices listed in Table 1.

### 3.3 HDG operator in three dimensions

Equation (28) defines the element contributions to the global LDG operator. Application of a SCHUR complement eliminates  $\mathbf{u}$  and  $\vec{\mathbf{q}}$  on a per-element basis and leads to an equation system of the form (11) with the element operator becoming

$$\mathbf{K}_e = \mathbf{G}_e - \mathbf{R}_e^T \mathbf{A}_e^{-1} \mathbf{R}_e. \quad (31)$$



Table 1: System matrices occurring in a three-dimensional LDG formulation on Cartesian tensor-product elements expressed using the standard element matrices stemming from (8). For the tensor-product structure, the vectors  $\tilde{\mathbf{u}}_{i,e}$  have the shape  $2 \times (p+1) \times (p+1)$ ,  $(p+1) \times 2 \times (p+1)$ , and  $(p+1) \times (p+1) \times 2$  for the  $x_1$ ,  $x_2$ , and  $x_3$  direction, respectively.

Matrix	Definition	Matrix	Definition
$\mathbf{M}_e$	$d_{0,e} \mathbf{M} \otimes \mathbf{M} \otimes \mathbf{M}$	$\mathbf{E}_e$	$\mathbf{E}_{1,e} + \mathbf{E}_{2,e} + \mathbf{E}_{3,e}$
$\mathbf{D}_{1,e}$	$h_{1,e}/2 d_{1,e} \mathbf{M} \otimes \mathbf{M} \otimes \mathbf{D}$	$\mathbf{E}_{1,e}$	$d_{1,e} \mathbf{M} \otimes \mathbf{M} \otimes \mathbf{E}$
$\mathbf{D}_{2,e}$	$h_{2,e}/2 d_{2,e} \mathbf{M} \otimes \mathbf{D} \otimes \mathbf{M}$	$\mathbf{E}_{2,e}$	$d_{2,e} \mathbf{M} \otimes \mathbf{E} \otimes \mathbf{M}$
$\mathbf{D}_{3,e}$	$h_{3,e}/2 d_{3,e} \mathbf{D} \otimes \mathbf{M} \otimes \mathbf{M}$	$\mathbf{E}_{3,e}$	$d_{3,e} \mathbf{E} \otimes \mathbf{M} \otimes \mathbf{M}$
$\mathbf{G}_{1,e}$	$d_{1,e} \mathbf{M} \otimes \mathbf{M} \otimes \mathbf{G}$		
$\mathbf{G}_{2,e}$	$d_{2,e} \mathbf{M} \otimes \mathbf{G} \otimes \mathbf{M}$		
$\mathbf{G}_{3,e}$	$d_{3,e} \mathbf{G} \otimes \mathbf{M} \otimes \mathbf{M}$		
$\mathbf{B}_{1,e}$	$d_{1,e} \mathbf{M} \otimes \mathbf{M} \otimes \mathbf{B}$	$\mathbf{C}_{1,e}$	$h_{1,e}/2 d_{1,e} \mathbf{M} \otimes \mathbf{M} \otimes \mathbf{C}$
$\mathbf{B}_{2,e}$	$d_{2,e} \mathbf{M} \otimes \mathbf{B} \otimes \mathbf{M}$	$\mathbf{C}_{2,e}$	$h_{2,e}/2 d_{2,e} \mathbf{M} \otimes \mathbf{C} \otimes \mathbf{M}$
$\mathbf{B}_{3,e}$	$d_{3,e} \mathbf{B} \otimes \mathbf{M} \otimes \mathbf{M}$	$\mathbf{C}_{3,e}$	$h_{3,e}/2 d_{3,e} \mathbf{C} \otimes \mathbf{M} \otimes \mathbf{M}$

The matrices  $\mathbf{G}_e$  and  $\mathbf{R}_e^T$  constitute the last three rows of the element operator in (28):

$$\mathbf{R}_e^T = \begin{pmatrix} \mathbf{B}_{1,e}^T & \mathbf{C}_{1,e}^T & \mathbf{0} & \mathbf{0} \\ \mathbf{B}_{2,e}^T & \mathbf{0} & \mathbf{C}_{2,e}^T & \mathbf{0} \\ \mathbf{B}_{3,e}^T & \mathbf{0} & \mathbf{0} & \mathbf{C}_{3,e}^T \end{pmatrix} \quad (32)$$

$$\mathbf{G}_e = \begin{pmatrix} \mathbf{G}_{1,e} & \mathbf{0} & \mathbf{0} \\ \mathbf{0} & \mathbf{G}_{2,e} & \mathbf{0} \\ \mathbf{0} & \mathbf{0} & \mathbf{G}_{3,e} \end{pmatrix} . \quad (33)$$

Here,  $\mathbf{G}_e$  is block diagonal and integrates separately over each of the six faces and  $\mathbf{R}_e$  computes the effect of the fluxes  $\tilde{\mathbf{u}}_i$  onto  $\mathbf{u}$  and each  $\mathbf{q}_i$  in the element. The matrix  $\mathbf{A}_e$  couples  $\mathbf{u}$  and  $\tilde{\mathbf{q}}$  in the element and is an extension of (14)

$$\mathbf{A}_e = \begin{pmatrix} \lambda \mathbf{M}_e + \mathbf{E}_e & -\mathbf{D}_{1,e} & -\mathbf{D}_{2,e} & -\mathbf{D}_{3,e} \\ -\mathbf{D}_{1,e}^T & -\mathbf{M}_e & \mathbf{0} & \mathbf{0} \\ -\mathbf{D}_{2,e}^T & \mathbf{0} & -\mathbf{M}_e & \mathbf{0} \\ -\mathbf{D}_{3,e}^T & \mathbf{0} & \mathbf{0} & -\mathbf{M}_e \end{pmatrix} . \quad (34)$$

As before, a SCHUR complement allows to compute an operator coupling only  $\mathbf{u}$  with itself which takes the form

$$\mathbf{Z}_{3D,e}^{-1} = \lambda d_{0,e} \mathbf{M} \otimes \mathbf{M} \otimes \mathbf{M} + d_{1,e} \mathbf{M} \otimes \mathbf{M} \otimes \mathbf{L} + d_{2,e} \mathbf{M} \otimes \mathbf{L} \otimes \mathbf{M} + d_{3,e} \mathbf{L} \otimes \mathbf{M} \otimes \mathbf{M} , \quad (35)$$

leading to the inverse

$$\mathbf{A}_e^{-1} = \mathbf{P}_e^T \mathbf{Z}_{3D,e} \mathbf{P}_e - \begin{pmatrix} \mathbf{0} & \mathbf{0} & \mathbf{0} & \mathbf{0} \\ \mathbf{0} & \mathbf{M}_e^{-1} & \mathbf{0} & \mathbf{0} \\ \mathbf{0} & \mathbf{0} & \mathbf{M}_e^{-1} & \mathbf{0} \\ \mathbf{0} & \mathbf{0} & \mathbf{0} & \mathbf{M}_e^{-1} \end{pmatrix} , \quad (36)$$

where

$$\mathbf{P}_e = \begin{pmatrix} \mathbf{I} \otimes \mathbf{I} \otimes \mathbf{I} \\ -\frac{2}{h_{1,e}} \mathbf{I} \otimes \mathbf{I} \otimes (\mathbf{M}^{-1} \mathbf{D}^T) \\ -\frac{2}{h_{2,e}} \mathbf{I} \otimes (\mathbf{M}^{-1} \mathbf{D}^T) \otimes \mathbf{I} \\ -\frac{2}{h_{3,e}} (\mathbf{M}^{-1} \mathbf{D}^T) \otimes \mathbf{I} \otimes \mathbf{I} \end{pmatrix}^T. \quad (37)$$

The combination of (31), (35), and (36) allows for a tensor-product evaluation of the HDG element operator, albeit one scaling with  $\mathcal{O}(p^4)$ .

## 4 A linearly scaling HDG operator in three dimensions

### 4.1 Sum factorization of the HDG operator

Using the operators from Table 1, all suboperators occurring in (31) can be expressed as tensor products. Similarly to (12), two operations are present: The matrix  $\mathbf{G}_e$  integrates the fluxes on each element boundary and is block-diagonal and, for a basis with a non-diagonal mass matrix, can be implemented in  $\mathcal{O}(n_p^3)$  multiplications, whereas a diagonal mass matrix streamlines it to  $\mathcal{O}(n_p^2)$ . Therefore, this part of the operator scales linearly already. The hybridized term, however, requires a closer look.

Typically, the operator gets evaluated by first applying  $\mathbf{R}_e$ , then  $\mathbf{A}_e^{-1}$  and, lastly, mapping back [38]. The application of  $\mathbf{A}_e^{-1}$  is often sped up using an extension of the generalized eigenvalue decomposition (18): the fast diagonalization technique from [8, 30]

$$\mathbf{Z}_{3D,e} = (\mathbf{S} \otimes \mathbf{S} \otimes \mathbf{S}) \mathbf{D}_{\mathbf{Z}_{3D,e}}^{-1} \underbrace{(\mathbf{S}^T \otimes \mathbf{S}^T \otimes \mathbf{S}^T)}_{\mathbf{S}_e^T} \quad (38a)$$

$$\mathbf{D}_{\mathbf{Z}_{3D,e}} = \lambda d_{0,e} \mathbf{I} \otimes \mathbf{I} \otimes \mathbf{I} + d_{1,e} \mathbf{I} \otimes \mathbf{I} \otimes \mathbf{\Lambda} + d_{2,e} \mathbf{I} \otimes \mathbf{\Lambda} \otimes \mathbf{I} + d_{3,e} \mathbf{\Lambda} \otimes \mathbf{I} \otimes \mathbf{I} \quad , \quad (38b)$$

where  $\mathbf{S}$  and  $\mathbf{\Lambda}$  are the same as in the one-dimensional case, i.e. (18). However, the application of the three-dimensional tensor product  $\mathbf{S} \otimes \mathbf{S} \otimes \mathbf{S}$  still requires  $\mathcal{O}(p^4)$  operations and, hence, must be eliminated to lower the operation count to  $\mathcal{O}(n_{\text{DOF}}) = \mathcal{O}(p^3 n_e)$ . Here, a similar strategy as in [18] proved sufficient: Instead of using the operators  $\mathbf{R}_e$ ,  $\mathbf{P}_e$ , and  $\mathbf{S} \otimes \mathbf{S} \otimes \mathbf{S}$  one after the other, they are fused together using (27b). This results in an operator mapping directly from the faces into the element eigenspace, where  $\mathbf{D}_{\mathbf{Z}_{3D,e}}^{-1}$  can be applied, and then mapping back from the eigenspace directly to the faces. As in the one-dimensional case, the approach requires an explicit form of  $\mathbf{B}_{S,e} = \mathbf{S}_e^T \mathbf{P}_e \mathbf{R}_e$ , which computes to

$$\mathbf{B}_{S,e} = \begin{pmatrix} d_{1,e} \mathbf{S}^T \mathbf{M} \otimes \mathbf{S}^T \mathbf{M} \otimes \mathbf{B}_S & d_{2,e} \mathbf{S}^T \mathbf{M} \otimes \mathbf{B}_S \otimes \mathbf{S}^T \mathbf{M} & d_{3,e} \mathbf{B}_S \otimes \mathbf{S}^T \mathbf{M} \otimes \mathbf{S}^T \mathbf{M} \end{pmatrix}. \quad (39)$$

Using the above representation, the HDG element operator simplifies as follows

$$\begin{aligned} \mathbf{K}_e &= \mathbf{G}_e - \mathbf{R}_e^T \mathbf{A}_e^{-1} \mathbf{R}_e \\ \Rightarrow \mathbf{K}_e &= \mathbf{G}_e + \mathbf{R}_e^T \begin{pmatrix} \mathbf{0} & \mathbf{0} & \mathbf{0} & \mathbf{0} \\ \mathbf{0} & \mathbf{M}_e^{-1} & \mathbf{0} & \mathbf{0} \\ \mathbf{0} & \mathbf{0} & \mathbf{M}_e^{-1} & \mathbf{0} \\ \mathbf{0} & \mathbf{0} & \mathbf{0} & \mathbf{M}_e^{-1} \end{pmatrix} \mathbf{R}_e - \mathbf{R}_e^T \mathbf{P}_e^T \mathbf{Z}_e^{-1} \mathbf{P}_e \mathbf{R}_e \\ \Rightarrow \mathbf{K}_e &= \mathbf{G}_e + \begin{pmatrix} \mathbf{C}_{1,e}^T \mathbf{M}_e^{-1} \mathbf{C}_{1,e} & \mathbf{0} & \mathbf{0} \\ \mathbf{0} & \mathbf{C}_{2,e}^T \mathbf{M}_e^{-1} \mathbf{C}_{2,e} & \mathbf{0} \\ \mathbf{0} & \mathbf{0} & \mathbf{C}_{3,e}^T \mathbf{M}_e^{-1} \mathbf{C}_{3,e} \end{pmatrix} - \mathbf{B}_{S,e}^T \mathbf{D}_{\mathbf{Z}_{3D,e}}^{-1} \mathbf{B}_{S,e}. \end{aligned} \quad (40)$$

---

**Algorithm 2** Computation of the effect of the HDG operator on a per-element basis in the three-dimensional case, called  $\tilde{\mathbf{r}}$ , from the current flux  $\tilde{\mathbf{u}}$ . For the tensor-product structure, the vectors  $\tilde{\mathbf{u}}_{i,e}$  have the size  $2 \times (p+1) \times (p+1)$ ,  $(p+1) \times 2 \times (p+1)$ , and  $(p+1) \times (p+1) \times 2$  for the  $x_1$ ,  $x_2$ , and  $x_3$  direction, respectively.

---

```

function HDG_OP_3D( $\tilde{\mathbf{u}}$ )
  for  $e = 1, n_e$  do
     $\mathbf{F}_E \leftarrow$   $(\mathbf{S}^T \mathbf{M} \otimes \mathbf{S}^T \mathbf{M} \otimes \mathbf{B}_S)$   $d_{1,e} \tilde{\mathbf{u}}_{1,e}$  ▷  $x_1$  contribution to  $\mathbf{F}_E$ 
       $+$   $(\mathbf{S}^T \mathbf{M} \otimes \mathbf{B}_S \otimes \mathbf{S}^T \mathbf{M})$   $d_{2,e} \tilde{\mathbf{u}}_{2,e}$  ▷  $x_2$  contribution to  $\mathbf{F}_E$ 
       $+$   $(\mathbf{B}_S \otimes \mathbf{S}^T \mathbf{M} \otimes \mathbf{S}^T \mathbf{M})$   $d_{3,e} \tilde{\mathbf{u}}_{3,e}$  ▷  $x_3$  contribution to  $\mathbf{F}_E$ 
     $\mathbf{u}_E \leftarrow \mathbf{D}_{\mathbf{z}_{3D,e}}^{-1} \mathbf{F}_E$  ▷ solution in eigenspace
     $\tilde{\mathbf{r}}_{1,e} \leftarrow d_{1,e} \mathbf{M} \otimes \mathbf{M} \otimes (\mathbf{G} + \mathbf{C}^T \mathbf{M}^{-1} \mathbf{C}) \tilde{\mathbf{u}}_{1,e} - d_{1,e} (\mathbf{M} \mathbf{S} \otimes \mathbf{M} \mathbf{S} \otimes \mathbf{B}_S^T) \mathbf{u}_E$ 
     $\tilde{\mathbf{r}}_{2,e} \leftarrow d_{2,e} \mathbf{M} \otimes (\mathbf{G} + \mathbf{C}^T \mathbf{M}^{-1} \mathbf{C}) \otimes \mathbf{M} \tilde{\mathbf{u}}_{2,e} - d_{2,e} (\mathbf{M} \mathbf{S} \otimes \mathbf{B}_S^T \otimes \mathbf{M} \mathbf{S}) \mathbf{u}_E$ 
     $\tilde{\mathbf{r}}_{3,e} \leftarrow d_{3,e} (\mathbf{G} + \mathbf{C}^T \mathbf{M}^{-1} \mathbf{C}) \otimes \mathbf{M} \otimes \mathbf{M} \tilde{\mathbf{u}}_{3,e} - d_{3,e} (\mathbf{B}_S^T \otimes \mathbf{M} \mathbf{S} \otimes \mathbf{M} \mathbf{S}) \mathbf{u}_E$ 
  end for
  return  $\tilde{\mathbf{r}}$ 
end function

```

---

The first two terms implement the interaction between opposing faces of the element, using  $\mathcal{O}(p^3)$  multiplications for a non-diagonal mass matrix and  $\mathcal{O}(p^2)$  for a diagonal one. The last term applies  $\mathbf{B}_{S,e}$ , with  $\mathcal{O}(p^3)$  multiplications when using  $\mathbf{S}^T \mathbf{M} \otimes \mathbf{S}^T \mathbf{M}$  on the faces and then expanding into the element eigenspace, then  $\mathbf{D}_{\mathbf{z}_{3D,e}}^{-1}$  in  $(p+1)^3$  multiplications and, lastly, maps back with  $\mathbf{B}_{S,e}^T$ , also using  $\mathcal{O}(p^3)$  multiplications when reducing to the faces first. Therefore, the operator can be applied in linear runtime, achieving linear scaling and, therefore, a major goal of the paper.

Algorithm 2 depicts an implementation of the operator which expands Algorithm 1 to three-dimensional cuboidal tensor-product elements. In every element, the six faces infer a residual for  $\mathbf{u}$  in the eigenspace E, called  $\mathbf{F}_E$ . There, the inverse eigenvalues are applied to compute the inferred solution  $\mathbf{u}_E$ . Lastly, the effect of this eigenspace solution and the interaction between the opposing faces is computed, resulting in the overall residual  $\tilde{\mathbf{r}}_e$ .

Computing the right-hand side in the element eigenspace in Algorithm 2 requires  $24n_p^3$  floating point operations when applying  $\mathbf{S}^T \mathbf{M}$ , and further  $12n_p^3$  operations for mapping into the eigenspace. The application of  $\mathbf{D}_{\mathbf{z}_{3D,e}}^{-1}$  incurs another  $n_p^3$  operations, and mapping back leads to another  $36n_p^3$ . Compared to these  $73n_p^3$  operations, the two other terms remain insignificant: Assuming a diagonal mass matrix, as present for LEGENDRE polynomials, LAGRANGE polynomials on GAUSS points, or when approximating the mass matrix for LAGRANGE polynomials on GAUSS-LOBATTO nodes, the first two terms in (40) only require  $\mathcal{O}(p^2)$  operations.

## 4.2 Product factorization of the HDG operator

Algorithm 2 allows for an evaluation of the HDG residual in linear runtime. However, the application cost is high when compared to a tensor-product operator for the primal form of DG [36, 29]. Of the  $73n_p^3$  operations, most apply only the two transformations, either  $\mathbf{S}^T \mathbf{M} \otimes \mathbf{S}^T \mathbf{M}$  or  $\mathbf{M} \mathbf{S} \otimes \mathbf{M} \mathbf{S}$ . These can, however, be removed by transforming the operator. Consider the element operator mapping from the first direction to the first

---

**Algorithm 3** Computation of the effect of the HDG operator on a per-element basis for the transformed basis in the three-dimensional case, called  $\hat{\mathbf{r}}$ , from the transformed flux  $\hat{\mathbf{u}}$ .

---

```

function HDG_OP_3D( $\hat{\mathbf{u}}$ )
  for  $e = 1, n_e$  do
     $\mathbf{F}_E \leftarrow (\mathbf{I} \otimes \mathbf{I} \otimes \mathbf{B}_S) d_{1,e} \hat{\mathbf{u}}_{1,e} + (\mathbf{I} \otimes \mathbf{B}_S \otimes \mathbf{I}) d_{2,e} \hat{\mathbf{u}}_{2,e} + (\mathbf{B}_S \otimes \mathbf{I} \otimes \mathbf{I}) d_{3,e} \hat{\mathbf{u}}_{3,e}$ 
     $\mathbf{u}_E \leftarrow \mathbf{D}_{\mathbf{Z}_{3D,e}}^{-1} \mathbf{F}_E$ 
     $\hat{\mathbf{r}}_{1,e} \leftarrow d_{1,e} \mathbf{I} \otimes \mathbf{I} \otimes (\mathbf{G} + \mathbf{C}^T \mathbf{M}^{-1} \mathbf{C}) \hat{\mathbf{u}}_{1,e} - d_{1,e} (\mathbf{I} \otimes \mathbf{I} \otimes \mathbf{B}_S^T) \mathbf{u}_E$ 
     $\hat{\mathbf{r}}_{2,e} \leftarrow d_{2,e} \mathbf{I} \otimes (\mathbf{G} + \mathbf{C}^T \mathbf{M}^{-1} \mathbf{C}) \otimes \mathbf{I} \hat{\mathbf{u}}_{2,e} - d_{2,e} (\mathbf{I} \otimes \mathbf{B}_S^T \otimes \mathbf{I}) \mathbf{u}_E$ 
     $\hat{\mathbf{r}}_{3,e} \leftarrow d_{3,e} (\mathbf{G} + \mathbf{C}^T \mathbf{M}^{-1} \mathbf{C}) \otimes \mathbf{I} \otimes \mathbf{I} \hat{\mathbf{u}}_{3,e} - d_{3,e} (\mathbf{B}_S^T \otimes \mathbf{I} \otimes \mathbf{I}) \mathbf{u}_E$ 
  end for
  return  $\hat{\mathbf{r}}$ 
end function

```

---

direction

$$\begin{aligned} \mathbf{K}_{11,e} &= d_{1,e} \mathbf{M} \otimes \mathbf{M} \otimes (\mathbf{G} + \mathbf{C}^T \mathbf{M}^{-1} \mathbf{C}) \\ &\quad - d_{1,e} (\mathbf{M} \mathbf{S} \otimes \mathbf{M} \mathbf{S} \otimes \mathbf{B}_S^T) \mathbf{D}_{\mathbf{Z}_{3D,e}}^{-1} (\mathbf{S}^T \mathbf{M} \otimes \mathbf{S}^T \mathbf{M} \otimes \mathbf{B}_S) d_{1,e} \quad . \end{aligned} \quad (41)$$

Applying  $\mathbf{S}^T \otimes \mathbf{S}^T \otimes \mathbf{I}$  from the left and  $\mathbf{S} \otimes \mathbf{S} \otimes \mathbf{I}$  from the right leads to

$$\hat{\mathbf{K}}_{11,e} = (\mathbf{S}^T \otimes \mathbf{S}^T \otimes \mathbf{I}^T) \mathbf{K}_{11,e} (\mathbf{S} \otimes \mathbf{S} \otimes \mathbf{I}) \quad (42)$$

$$\begin{aligned} \hat{\mathbf{K}}_{11,e} &= (\mathbf{S}^T \otimes \mathbf{S}^T \otimes \mathbf{I}) [d_{1,e} \mathbf{M} \otimes \mathbf{M} \otimes (\mathbf{G} + \mathbf{C}^T \mathbf{M}^{-1} \mathbf{C})] (\mathbf{S} \otimes \mathbf{S} \otimes \mathbf{I}) \\ &\quad - d_{1,e} \left[ (\mathbf{S}^T \otimes \mathbf{S}^T \otimes \mathbf{I}) (\mathbf{M} \mathbf{S} \otimes \mathbf{M} \mathbf{S} \otimes \mathbf{B}_S^T) \mathbf{D}_{\mathbf{Z}_{3D,e}}^{-1} (\mathbf{S}^T \mathbf{M} \otimes \mathbf{S}^T \mathbf{M} \otimes \mathbf{B}_S) (\mathbf{S} \otimes \mathbf{S} \otimes \mathbf{I}) \right] d_{1,e} \end{aligned} \quad (43)$$

$$\begin{aligned} \Rightarrow \hat{\mathbf{K}}_{11,e} &= d_{1,e} [\mathbf{S}^T \mathbf{M} \mathbf{S} \otimes \mathbf{S}^T \mathbf{M} \mathbf{S} \otimes (\mathbf{G} + \mathbf{C}^T \mathbf{M}^{-1} \mathbf{C})] \\ &\quad - d_{1,e} \left[ (\mathbf{S}^T \mathbf{M} \mathbf{S} \otimes \mathbf{S}^T \mathbf{M} \mathbf{S} \otimes \mathbf{B}_S^T) \mathbf{D}_{\mathbf{Z}_{3D,e}}^{-1} (\mathbf{S}^T \mathbf{M} \mathbf{S} \otimes \mathbf{S}^T \mathbf{M} \mathbf{S} \otimes \mathbf{B}_S) \right] d_{1,e} \end{aligned} \quad (44)$$

The identity  $\mathbf{S}^T \mathbf{M} \mathbf{S} = \mathbf{I}$  from (18a) simplifies these terms to

$$\hat{\mathbf{K}}_{11,e} = d_{1,e} \mathbf{I} \otimes \mathbf{I} \otimes (\mathbf{G} + \mathbf{C}^T \mathbf{M}^{-1} \mathbf{C}) - d_{1,e} (\mathbf{I} \otimes \mathbf{I} \otimes \mathbf{B}_S^T) \mathbf{D}_{\mathbf{Z}_{3D,e}}^{-1} (\mathbf{I} \otimes \mathbf{I} \otimes \mathbf{B}_S) d_{1,e} \quad . \quad (45)$$

The terms for the faces in the  $x_2$  and  $x_3$  direction can be treated similarly by permutation of  $\mathbf{S}^T \otimes \mathbf{S}^T \otimes \mathbf{I}$ , as can terms coupling different directions. Therefore, every occurrence of  $\mathbf{S}^T \mathbf{M}$  in the operator becomes  $\mathbf{S}^T \mathbf{M} \mathbf{S} = \mathbf{I}$ , and similarly  $\mathbf{M} \mathbf{S}$  and  $\mathbf{M}$  transform to identity as well. While the transformation can simplify the implementation of Algorithm 2, applying the transformation to solution variable and residual instead lowers the operator costs across the whole solution process.

Algorithm 3 depicts the resulting algorithm. Not only does the operator now mainly consist of the mapping from the transformed faces into the element eigenspace and back, requiring  $25n_p^3$  multiplications, the terms coupling opposing faces now use  $\mathcal{O}(p^2)$  in every basis, independent of the mass matrix. While the algorithm requires transformation of the coefficients for the flux  $\tilde{\mathbf{u}} \rightarrow \hat{\mathbf{u}}$  prior to the application, this can be done after computing the right-hand side for fluxes and, therefore, as a tensor-product operation on the faces, requiring  $\mathcal{O}(p^3)$  operations.

### 4.3 Operator runtimes

While the multiplication count constitutes a good measure for the asymptotic performance of an algorithm, it is typically insufficient to predict the efficiency attained in practice.

Table 2: Application and preprocessing costs for the operators in conjunction with the incurred number of loads and stores per operator evaluation. Here, CCG denotes the condensed continuous GALERKIN method, whereas HDG denotes the hybridized discontinuous GALERKIN method. For the condensed case, a factor of three was imposed on the loads and stores of to account for the evaluation of the primary part.

Operator	Preprocessing cost	# FLOP	# loads / stores
CCG-MM	$\mathcal{O}(p^5)$	$72(p-1)^4 + \mathcal{O}(p^2)$	$3 \cdot 18(p-1)^2$
CCG-TP	$\mathcal{O}(p^3)$	$97(p-1)^3 + \mathcal{O}(p^2)$	$3 \cdot 18(p-1)^2 + (p-1)^3$
CCG-TPT	$\mathcal{O}(p^3)$	$25(p-1)^3 + \mathcal{O}(p^2)$	$3 \cdot 18(p-1)^2 + (p-1)^3$
HDG-TP	$\mathcal{O}(p^3)$	$73(p+1)^3 + \mathcal{O}(p^2)$	$18(p+1)^2 + (p+1)^3$
HDG-TPT	$\mathcal{O}(p^3)$	$25(p+1)^3 + \mathcal{O}(p^2)$	$18(p+1)^2 + (p+1)^3$

For instance, matrix-matrix multiplications require more operations than tensor-products, but can remain faster over a wide range of polynomial degrees [3, 23]. Therefore, runtime tests were conducted to validate both, that the linear scaling is achieved as well as that matrix-matrix implementations are outperformed.

Two variants of the HDG element operator were considered. The first implemented Algorithm 2 for GAUSS-LOBATTO-LEGENDRE (GLL) polynomials. As it implements a HDG operator using tensor products it was called HDG-TP. The second one implemented Algorithm 3, which utilizes a transformation to streamline the operation count, and was therefore named HDG-TPT. Variants for the statically condensed continuous Galerkin case (CCG) implementing the static condensed operator served as reference. The first thereof implemented the condensed part using one matrix-matrix multiplication and was, therefore, called CCG-MM. The two other variants used a tensor-product decomposition, the first one on GLL polynomials, called CCG-TP, and the second one, CCG-TPT, using a transformed coordinate system and thereby lowering the number of operations. Derivations of these can be found in [20, 22]. The matrix-matrix-based operator required  $\mathcal{O}(p^4)$  operations, whereas  $\mathcal{O}(p^3)$  operations sufficed for all tensor-product-based operators. Table 2 lists the operators, leading factors of the operation counts, and associated preprocessing costs.

The operators were implemented in Fortran 2008 using double precision. The Intel Fortran compiler v. 2018 compiled the variants, with the associated MKL serving as BLAS implementation. A single core of an Intel Xeon E5-2680 v.3 constituted the measuring platform. As it ran with a clock speed of 2.5 GHz, it allowed for a maximum floating point rate of 40 GFLOP/s [13].

For every polynomial degree in  $\{2 \dots 32\}$ , the operators were used 101 times on  $n_e = 8^3$  spectral elements, with the runtime of the last 100 times being measured with `MPI_Wtime`. This approach precludes measurement of instantiation effects, for instance of libraries such as BLAS.

Figure 2 depicts the measured instantiation times and runtimes in combination with the achieved floating point rate and equivalent degrees of freedom per second. For the preparation time, the expected orders are achieved: Computing the assembled element matrix for the static condensed method CCG-MM scales with  $\mathcal{O}(p^5)$ . The preprocessing time of the other operators scales with  $\mathcal{O}(p^3)$ , which can be attributed to them only requiring solution of an eigenvalue problem and then computing the inverse eigenvalues, both scaling with  $\mathcal{O}(p^3 n_e)$ .

The runtimes of the operators, shown in Figure 2(b), fall into three categories. The first

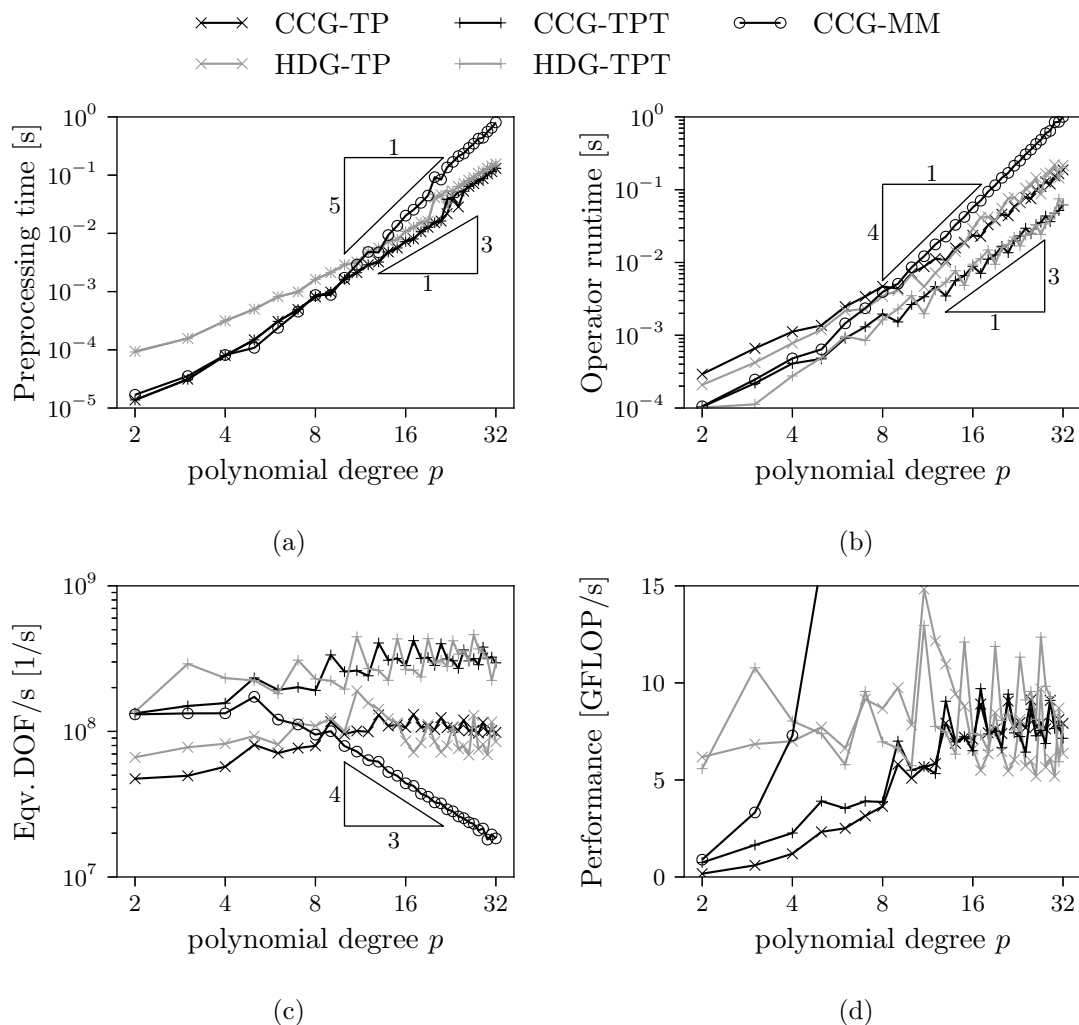


Figure 2: Operator runtimes when varying the polynomial degree  $p$  in a homogeneous mesh consisting of  $n_e = 8^3 = 512$  spectral elements. (a): Preparation times for the matrices used by the operators. (b): Operator runtimes. (c): Rate of updates per second, where the equivalent number of degrees of freedom is calculated to be  $(p + 1)^3 n_e$ . (d): Rate of floating point operations per second measured in GFLOP/s.

one consists of the matrix-matrix-based version CCG-MM. While attaining the highest rate of floating point operations, near 35 GFLOP/s beyond  $p = 8$ , the runtime increases significantly compared to the other methods, stemming from an increasing number of required operations per degree of freedom. This is reflected in the number of updated degrees of freedom which decreases substantially with  $p$ . The non-transformed operators HDG-TP and CCG-TP constitute the second category, generating a mostly constant rate of updates while exhibiting a smaller runtime than CCG-MM starting from  $p = 6$ . For large polynomial degrees the rate of updates oscillates depending on the polynomial degree. The maximum is achieved when the number of points per direction  $p + 1$  is a multiple of four, which lends itself to optimization for the given architecture, whereas slightly lower update rates result at other polynomial degrees. For CCG-TP the operator consists of a primary and a condensed part. The latter resembles the HDG operator and can be optimized well, but the former couples the vertices, edges, and faces of the element and consists of multiple smaller suboperators. While oscillations occurs, they are not as large as for HDG-TP.

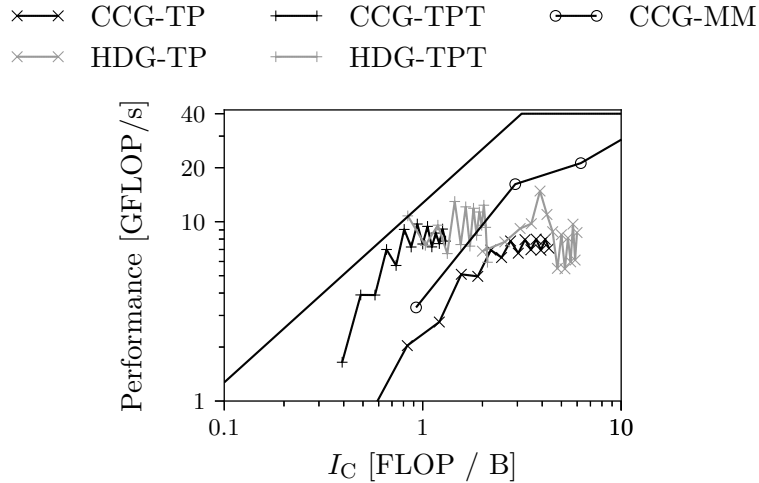


Figure 3: Roofline analysis of the operator variants, depicting the performance attained in practice over the computational intensity  $I_C$  resulting from Table 2. In the analysis, a limiting memory bandwidth of  $12.7 \text{ GB s}^{-1}$  and a maximum performance of  $40 \text{ GFLOP s}^{-1}$  are used, as measured in [13]. Furthermore, for clarity of presentation, only odd polynomial degrees are shown, as these result in even operator sizes.

Transforming the equation system allows leveraging the operators HDG-TPT and CCG-TPT. These are faster than CCG-MM for all polynomial degrees and gain a factor of four over the non-transformed variants. The HDG variant is slightly faster at lower polynomial degrees, due to the primary part of the condensed system being evaluated for CCG-TPT. For  $p > 4$ , however, both variants attain similar update rates, only at different polynomial degrees. With the tensor-product variants exhibiting a mostly constant rate of updates, a major goal has been achieved: operators scaling linearly with the number of degrees of freedom. Moreover, these attain the same degree of efficiency as the ones for the continuous discretization.

Lastly, Figure 2(d) depicts the rate of floating-point operations. All variants start with a relatively low rate. However, the rate increases quickly for the matrix-matrix variant, which attains more than  $15 \text{ GFLOP/s}$  at  $p = 5$  and saturates at  $35 \text{ GFLOP/s}$ , which is beyond the range shown here. These operations, however, are largely wasted since the number of updates decreases, as shown in Figure 2(c). Due to evaluating the primary part, the variants CCG-TP and CCG-TPT for the static condensed operator harness only one eighth of the compute power at  $p = 12$ , whereas the variants for HDG quickly use one quarter. Beyond  $p = 16$ , the HDG variants exhibit a highly oscillatory behaviour compared to the variants for static condensation. This is due to the very short, monolithic operators. These are far easier to optimize for the compiler, leading to spikes where the operator width is a multiple of the register width. All tensor-product operators attain only near a quarter of the maximum rate. This stems from the implementation, where the matrix of eigenvalues  $\mathbf{D}_{\mathbf{z}_{3D,e}}^{-1}$  is precomputed and stored explicitly. In a roofline analysis, as shown in Figure 3, the usage of  $\mathbf{D}_{\mathbf{z}_{3D,e}}^{-1}$  leads to a constant as asymptotic limit for the computational intensity [37]. However, while loading  $\mathcal{O}(p^3)$  floating point numbers, the operation is still far from being memory-bound when computing at high polynomial degrees. For machines with a lower critical computational intensity, computing the inverse eigenvalues in the operator itself can be a remedy, but was not found to be beneficial with

the CPUs utilized in this study, even when capitalizing on imprecise floating point division. However, the growing memory gap might render it beneficial in the future.

## 5 Construction of an elliptic solver with linear runtime

### 5.1 Linearly scaling face-local preconditioners

With a linearly scaling residual evaluation, the door to linearly scaling solvers is wide open. The only remaining obstacle is attaining a well-performing linearly scaling preconditioner. This requirement severely limits the possibilities. Assuming a constant iteration count, only tensor-product preconditioners working on the faces remain a possibility. In general, a multigrid approach leads to very efficient solvers, as done for the continuous discretization in [14, 24, 17]. There, SCHWARZ-type preconditioners using tensor-products were employed to generate an efficient smoother with linear scaling. The derivation of a linearly-scaling SCHWARZ-type smoother required for the multigrid algorithm is, however, a topic of its own and well beyond the scope of this paper.

To investigate the performance achievable with the linearly scaling operator, block-JACOBI methods are used. They proved highly efficient for solution of diffusion equations in semi-implicit time-stepping schemes [17] and provide an astonishing resilience against high aspect ratios [22]. Moreover, they include the same kind of operations found in SCHWARZ-type smoothers for multigrid and serve to evaluate their qualitative behaviour for high polynomial degrees. Due to these positive properties the same approach is employed here as well.

Two preconditioners are derived: The first one, applies the exact inverse on every face of the mesh, leading to a block-JACOBI preconditioner, whereas the second one only utilizes the inverse of the main diagonal. To derive the preconditioners, a single element  $\Omega_e$  is considered. The operator connecting two opposing faces, as illustrated here for the first direction, reads

$$\begin{aligned} \mathbf{K}_{11,e} &= d_{1,e} \mathbf{M} \otimes \mathbf{M} \otimes (\mathbf{G} + \mathbf{C}^T \mathbf{M}^{-1} \mathbf{C}) \\ &\quad - d_{1,e} (\mathbf{M} \mathbf{S} \otimes \mathbf{M} \mathbf{S} \otimes \mathbf{B}_S^T) \mathbf{D}_{\mathbf{Z}_{3D,e}}^{-1} (\mathbf{S}^T \mathbf{M} \otimes \mathbf{S}^T \mathbf{M} \otimes \mathbf{B}_S) d_{1,e} \quad . \end{aligned} \quad (46)$$

When removing the occurrences of  $\mathbf{M} \mathbf{S}$  by multiplying with  $\mathbf{S}^T$  from the left and  $\mathbf{S}$  from the right in both face directions, the operator becomes

$$\begin{aligned} \hat{\mathbf{K}}_{11,e} &= (\mathbf{S}^T \otimes \mathbf{S}^T \otimes \mathbf{I}) \mathbf{K}_{11,e} (\mathbf{S} \otimes \mathbf{S} \otimes \mathbf{I}) \\ &= d_{1,e} (\mathbf{I} \otimes \mathbf{I} \otimes \mathbf{G} + \mathbf{B}_S^T \mathbf{M}^{-1} \mathbf{B}_S) - d_{1,e} (\mathbf{I} \otimes \mathbf{I} \otimes \mathbf{B}_S^T) \mathbf{D}_{\mathbf{Z}_{3D,e}}^{-1} (\mathbf{I} \otimes \mathbf{I} \otimes \mathbf{B}_S) d_{1,e} \quad , \end{aligned} \quad (47)$$

which is diagonal in the two directions on the faces. As each face occurs in two elements, two elements contribute to the preconditioner. Let  $\mathbf{Y}_e$  denote the effect of  $\mathbf{K}_e$  from one face to itself for all faces. Then,  $\tilde{\mathbf{Y}} = \tilde{\mathbf{Q}} \tilde{\mathbf{Q}}^T \mathbf{Y}$  is the effect of the global flux of the face onto itself. However, the application requires the variable to reside in the face eigenspace, i.e. after applying the transformation matrix  $\mathbf{S}^T \mathbf{M}$  in the two directions of the face. Therefore, application of the preconditioner consists of first mapping into the face eigenspaces, applying the inverse  $\tilde{\mathbf{Y}}^{-1}$ , and then mapping back. Algorithm 4 shows an implementation thereof. The preconditioner requires four one-dimensional matrix products on each face, resulting in  $4 \cdot 2 \cdot 6n_p^3 = 48n_p^3 n_e$  floating point operations per application of the preconditioner. Moreover, as  $\hat{\mathbf{K}}_{ii,e}$  from (47) can be computed in  $\mathcal{O}(p^3)$  operations, determining  $\tilde{\mathbf{Y}}^{-1}$  requires  $\mathcal{O}(p^3 n_e)$  operations.



---

**Algorithm 4** Application of the block preconditioner to the residual  $\tilde{\mathbf{r}}$  in a non-transformed system. Here, all variables are stored and accessed in a face-wise fashion and  $n_F$  denote the total number of faces in the mesh.

---

```

function BLOCK_PRECONDITIONER( $\tilde{\mathbf{r}}$ )
  for  $f = 1, n_F$  do                                ▷ Loop over all faces
     $\hat{\mathbf{r}}_f \leftarrow (\mathbf{S}^T \otimes \mathbf{S}^T) \tilde{\mathbf{r}}_f$         ▷ transformation
     $\hat{\mathbf{z}}_f \leftarrow \tilde{\mathbf{Y}}_f^{-1} \hat{\mathbf{r}}_f$                 ▷ inversion on the faces
     $\tilde{\mathbf{z}}_f \leftarrow (\mathbf{S} \otimes \mathbf{S}) \hat{\mathbf{z}}_f$             ▷ transformation
  end for
  return  $\tilde{\mathbf{z}}$ 
end function

```

---

With Algorithm 4, an explicit representation for the inverse on the faces is present. However, the application costs are nearly as high as the operator costs. A diagonal preconditioner can solve the latter issue, at the expense of the condition of the system. To compute the diagonal preconditioner for one point  $i, j$  on a face, the restrictor  $\mathbf{e}_j \otimes \mathbf{e}_i$  can be utilized. The diagonal results via  $(\mathbf{e}_j \mathbf{S} \otimes \mathbf{e}_i \mathbf{S}) \tilde{\mathbf{Y}}^{-1} (\mathbf{S}^T \mathbf{e}_j^T \otimes \mathbf{S}^T \mathbf{e}_i^T)$ , which can be precomputed in  $\mathcal{O}(p^3)$  and applied in  $\mathcal{O}(p^2)$ .

## 5.2 Summary of solution method

So far only pieces of the solution process were shown. This subsection states the solution method as a whole. The solution process with HDG works as follows: First, hybridize the system by computing the fluxes  $\tilde{\mathbf{u}}$  from the initial guess for the solution variable  $\mathbf{u}$ , first, computing  $\mathbf{q}$  via (2b) and then using (4a). For a non-primal formulation, which includes the auxiliary variable  $\mathbf{q}$  as solution variable,  $\tilde{\mathbf{u}}$  can be computed directly via (4a). Thereafter, the right-hand side  $\mathbf{F}^{\text{HDG}}$  is computed from the right-hand side for  $\mathbf{u}$  and the boundary conditions. Solution of the HDG system (11) constitutes the third step. Lastly, the solution is recomputed from the flux. Algorithm 5 summarizes the solution algorithm.

In the solution process, the hybridization incurs a three-dimensional tensor product to transform  $\mathbf{u}$  into the element operator eigenspace. This step scales with  $\mathcal{O}(p^4 n_e)$ , as does the transformation of the right-hand side. But at least these occur only once. The solution process, when implemented with a CG method, consists of an operator evaluation followed by scalar products and a preconditioner application. When using the operator evaluation from Section 4 and preconditioners from Section 5.1, these are lowered in complexity from  $\mathcal{O}(p^4 n_e)$  to  $\mathcal{O}(p^3 n_e) = \mathcal{O}(n_{\text{DOF}})$ , i.e. the resulting solvers achieve a linearly scaling iteration time. The last step again requires a transformation into the element eigenspaces and, therefore,  $\mathcal{O}(p^4 n_e)$  operations. However, the pre- and postprocessing occur, by definition, once per solution process, whereas the iteration process is reiterated tens if not hundreds of times. For the continuous method, the iteration, not pre- and postprocessing are the most costly component for polynomial degrees up to  $p > 48$  [24], and these lie far outside the range of currently employed ones. Therefore, the solver can be described as scaling linearly for all relevant polynomial degrees.

The described algorithm works as is for the untransformed system. To leverage the product factorization from Section 4.2, a coordinate transformation is required, which gets prepended and appended to the solver call in Algorithm 5. As both of these operations can work on the already hybridized data and can be written in tensor-product form, they scale linearly with the overall number of degrees of freedom and do not impede the solution

---

**Algorithm 5** Solution process with HDG for a primal method.

---

```

function HDG_SOLVER(u, f)
  for  $e = 1, n_e$  do
     $\mathbf{q}_{1,e} \leftarrow d_{1,e} (\mathbf{I} \otimes \mathbf{I} \otimes \mathbf{D}) \mathbf{u}_e$             $\triangleright$  Compute  $\mathbf{q}_1$  via differentiation
     $\mathbf{q}_{2,e} \leftarrow d_{2,e} (\mathbf{I} \otimes \mathbf{D} \otimes \mathbf{I}) \mathbf{u}_e$             $\triangleright$  Compute  $\mathbf{q}_2$  via differentiation
     $\mathbf{q}_{3,e} \leftarrow d_{3,e} (\mathbf{D} \otimes \mathbf{I} \otimes \mathbf{I}) \mathbf{u}_e$             $\triangleright$  Compute  $\mathbf{q}_3$  via differentiation
     $\mathbf{F}_e^{\text{HDG}} \leftarrow \mathbf{g}_{N,e} + \mathbf{R}_e^T \mathbf{A}_e^{-1} (\mathbf{M}_e \mathbf{f}_e \quad \mathbf{0})^T$ 
  end for
   $\tilde{\mathbf{u}} \leftarrow \text{Flux}(\mathbf{u}, \mathbf{q})$                                 $\triangleright$  initial guess

  pCG_Solve( $\mathbf{K}\tilde{\mathbf{u}} = \mathbf{F}^{\text{HDG}}$ )                              $\triangleright$  solution with pCG method

  for  $e = 1, n_e$  do
     $\mathbf{F}_e \leftarrow (\mathbf{M}_e \mathbf{f}_e \quad \mathbf{0})^T + \mathbf{R}_e \tilde{\mathbf{u}}_e$             $\triangleright$  Right-hand side for  $\mathbf{u}$  and  $\mathbf{q}$ 
     $(\mathbf{u}_e \quad \mathbf{q}_e)^T \leftarrow \mathbf{A}_e^{-1} \mathbf{F}_e$                   $\triangleright$  Recompute solution variables
  end for
  return  $\mathbf{u}$ 
end function

```

---

**Algorithm 6** Solution process with HDG for the transformed system.

---

```

function TRANSFORMED_SOLVER( $\tilde{\mathbf{u}}, \mathbf{F}^{\text{HDG}}$ )
  for  $f = 1, n_F$  do
     $\hat{\mathbf{F}}_f^{\text{HDG}} \leftarrow (\mathbf{S}^T \otimes \mathbf{S}^T) \mathbf{F}_f^{\text{HDG}}$             $\triangleright$  transformed right-hand side
     $\hat{\tilde{\mathbf{u}}}_f \leftarrow (\mathbf{S}^T \mathbf{M} \otimes \mathbf{S}^T \mathbf{M}) \tilde{\mathbf{u}}_f$             $\triangleright$  transformed initial guess
  end for
  pCG_Solve( $\hat{\mathbf{K}}\hat{\tilde{\mathbf{u}}} = \hat{\mathbf{F}}^{\text{HDG}}$ )                              $\triangleright$  solution in transformed system
  for  $f = 1, n_F$  do
     $\tilde{\mathbf{u}}_f \leftarrow (\mathbf{S} \otimes \mathbf{S}) \hat{\tilde{\mathbf{u}}}_f$                     $\triangleright$  transformed initial guess
  end for
  return  $\tilde{\mathbf{u}}$ 
end function

```

---

process. Algorithm 6 summarizes the altered solver.

For testing purposes, four HDG solvers are considered, all leveraging the developed linear operators: The first one is a direct CG implementation of HDG without preconditioning and called HDG-unprec. The second one, HDG-diag, utilizes diagonal preconditioning. The third one, HDG-block, employs the block-preconditioner from Algorithm 4. The last considered HDG solver capitalizes on the transformation in Algorithm 6: The application of operator and preconditioner both require application of  $\mathbf{S}^T \mathbf{M}$  and  $\mathbf{S}^T$ , respectively, in the face directions before allowing for evaluation on the face. By applying these as coordinate transformation, Algorithm 3 can be used directly for evaluation. Moreover, the block preconditioner Algorithm 4 simplifies to a diagonal one. Hence, the transformation streamlines the operation count of both operator and block preconditioner, and the resulting solver is called HDG-trans. For all of these solvers, a counterpart using the continuous discretization with static condensation is investigated as well.

Table 3 lists the pre- and post-processing times for the solvers. For both, continuous and discontinuous discretization, the right-hand side results by applying an element-wise

Table 3: Number of operations for precomputation of matrices ( $N_{\text{mat}}$ ), pre- and post-processing of variables ( $N_{\text{prepost}}$ ), application of operator ( $N_{\text{op}}$ ) and application of the preconditioner ( $N_{\text{cond}}$ ) for the proposed solvers.

Solver	$N_{\text{mat}}$	$N_{\text{prepost}}$	$N_{\text{op}}$	$N_{\text{cond}}$
HDG-unprec	$\mathcal{O}(p^3 n_e)$	$\mathcal{O}(p^4 n_e)$	$73(p+1)^3 n_e$	–
HDG-diag	$\mathcal{O}(p^3 n_e)$	$\mathcal{O}(p^4 n_e)$	$73(p+1)^3 n_e$	$6(p+1)^2 n_e$
HDG-block	$\mathcal{O}(p^3 n_e)$	$\mathcal{O}(p^4 n_e)$	$73(p+1)^3 n_e$	$49(p+1)^3 n_e$
HDG-trans	$\mathcal{O}(p^3 n_e)$	$\mathcal{O}(p^4 n_e)$	$27(p+1)^3 n_e$	$6(p+1)^2 n_e$
CCG-unprec	$\mathcal{O}(p^3 n_e)$	$\mathcal{O}(p^4 n_e)$	$97(p-1)^3 n_e$	–
CCG-diag	$\mathcal{O}(p^3 n_e)$	$\mathcal{O}(p^4 n_e)$	$97(p-1)^3 n_e$	$6(p-1)^2 n_e$
CCG-block	$\mathcal{O}(p^3 n_e)$	$\mathcal{O}(p^4 n_e)$	$97(p-1)^3 n_e$	$49(p-1)^3 n_e$
CCG-trans	$\mathcal{O}(p^3 n_e)$	$\mathcal{O}(p^4 n_e)$	$25(p-1)^3 n_e$	$6(p-1)^2 n_e$

inverse via fast diagonalization. Similarly, the generation of the solution consists by mapping into the element eigenspace and applying a tensor-product to the solution there. These two operations scale with  $\mathcal{O}(p^4 n_e)$  and are only evaluated once during the solution process, such that they not impede the linear scaling. They are not expected to dominate the runtime behaviour until at least  $p > 48$  [24], allowing to disregard the issue here.

### 5.3 Definition of a test case for assessment

In the following the test case from [22] serves to evaluate the solvers derived in the previous section. In a domain  $\Omega = (0, 2\pi)^3$  the manufactured solution

$$u_{\text{ex}}(x) = \cos(k(x_1 - 3x_2 + 2x_3)) \sin(k(1 + x_1)) \cdot \sin(k(1 - x_2)) \sin(k(2x_1 + x_2)) \sin(k(3x_1 - 2x_2 + 2x_3)) \quad , \quad (48)$$

is considered, with the stiffness parameter  $k$  set to 5, and the right-hand side of (1a) analytically evaluated from

$$f(x) = \lambda u_{\text{ex}}(x) - \Delta u_{\text{ex}}(x) \quad . \quad (49)$$

Inhomogeneous DIRICHLET boundary conditions are used to impose the exact values, as defined by (48), on the boundary. The initial guess for  $\mathbf{u}$  consists of pseudo-random numbers in the interior of the domain, with the DIRICHLET conditions imposed on the boundary. This initial guess is used directly for the continuous discretization, whereas for HDG the initial fluxes resulting from the strong form of (4a) are imposed. While  $\lambda > 0$  was utilized in preliminary validations, the POISSON case  $\lambda = 0$  leads to a worse condition. This generates a system that is harder to solve and is, therefore, utilized here to demonstrate the performance for the worst case.

As in Section 4.3, the solvers were implemented in Fortran using double precision, compiled with the Intel Fortran compiler, and a single core of an Intel Xeon E5-2680 v3 constituted the measuring platform. On this machine, the solvers were run 11 times. The runtime of the last ten runs was measured with `MPI_Wtime`, whereas the first run precluded measurement of instantiation effects. In every run, the iterations were stopped after the initial residual was reduced by a factor of  $10^{-10}$ .

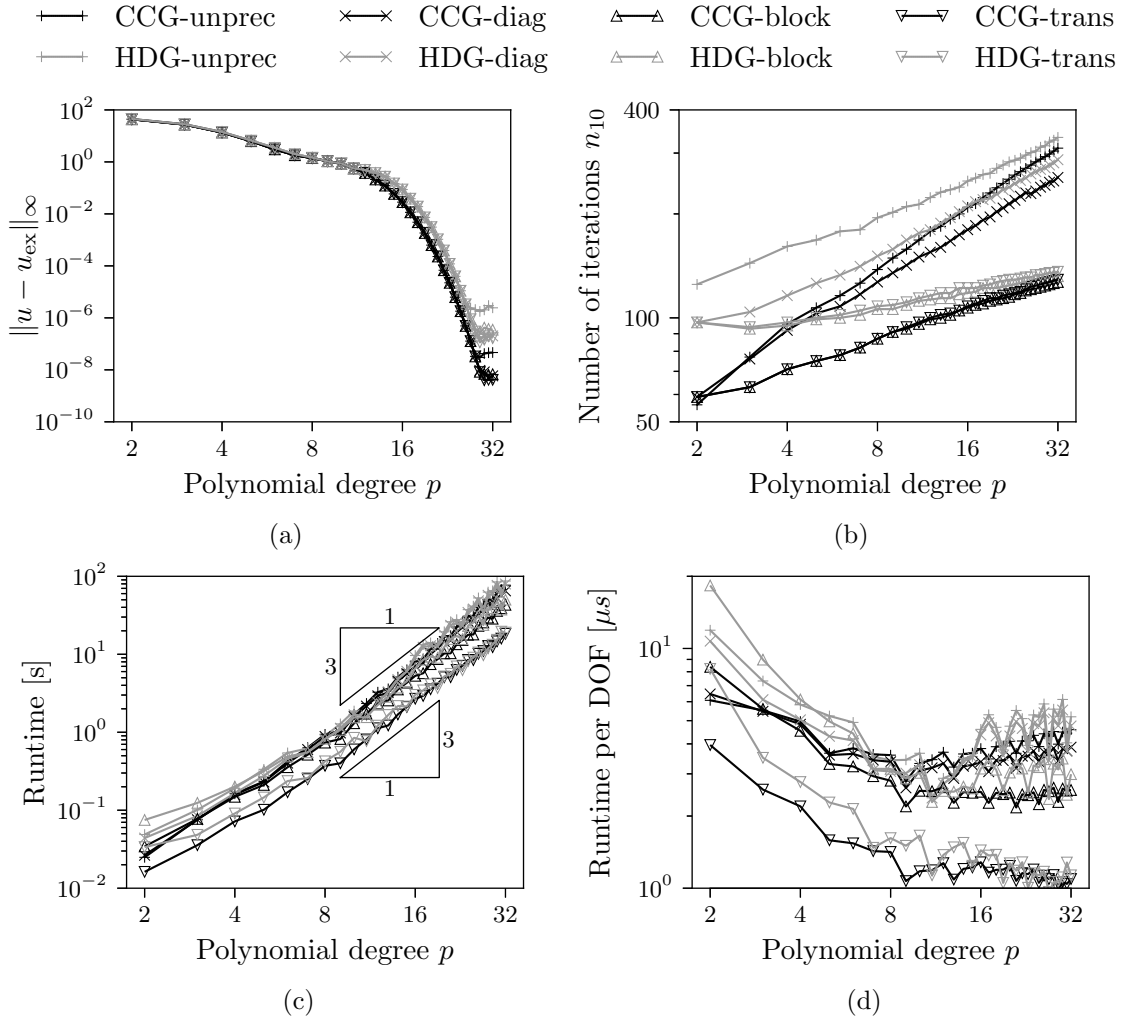


Figure 4: Results when varying the polynomial degree  $p$  in a homogeneous mesh consisting of  $n_e = 8^3$  spectral elements. For the HDG solvers, the penalty parameter was fixed at  $\tau_{e,i} = 25$ . (a): Resulting discretization error. (b): Number of iterations required to lower the residual by ten orders. (c): Solver runtimes. (d): Runtimes per unknown.

#### 5.4 Robustness against increase in polynomial degree

The first test uses a constant number of elements  $n_e = 8^3 = 512$  while varying the polynomial degree in  $p \in \{2 \dots 32\}$ , with the penalty parameter set to  $\tau_e = 25$ .

Figure 4 depicts the solution error, the resulting number of iterations, the runtime, and the runtime per iteration and unknown. The error of all computed solutions behaves as it should. With the given number of elements and smaller polynomial degrees the discrete solution is not yet in the convergence range for this value of the stiffness parameter. Beyond  $p \approx 12$  spectral convergence is noticed, reflected by an increasing slope with increasing  $p$ , validating the discretization and solution procedures. Beyond a value of  $p \approx 26$  to  $p \approx 30$  the error saturates for all methods. The latter behaviour is common with high-order methods and results from a limited machine accuracy in combination with an accumulation of round-off errors. The level at which this occurs depends on the method. Here, the discontinuous discretization exhibits a somewhat higher error level compared to the continuous one. Furthermore, a difference between the unpreconditioned, and pre-

conditioned variants occurs: The former have a higher remaining error, which can stem from the combination of preconditioning in conjunction with a CG algorithm that does not include a restart, possibly leading to an accumulation of round-off errors and searches in the wrong subspace [33].

When comparing the number of iterations in Figure 4(b), HDG always requires more than the continuous formulation. For a low polynomial degree, a factor of two is present, whereas continuous and discontinuous variants converge against each other for high polynomial degrees. This indicates that the HDG has a worse condition number, stemming from a combination of more degrees of freedom and the ill-conditioned penalty terms, which dominate until high polynomial degrees.

As to be expected, a diagonal preconditioner for HDG results in a lower required number of iterations compared to the unpreconditioned version. The gain remains, however, small. In contrast, the block-preconditioner leads to a significant improvement, with  $\approx 100$  iterations being required over a wide range of polynomial degrees, and a factor of two less iterations at  $p = 32$ . While the number of iterations remains higher than in the continuous case for  $p < 16$ , the difference vanishes when further increasing the order.

Figure 4(c) depicts the runtimes. The unpreconditioned and diagonally-preconditioned solvers incur the highest runtime per degree of freedom, with the benefit of diagonal preconditioning mostly being offset by the higher costs. The block-preconditioned versions in the non-transformed systems, in contrast, exhibit a constant runtime per degree of freedom for  $p \geq 8$ , which lies near  $2.5 \mu\text{s}$  per degree of freedom, as shown in Figure 4(d). Therefore, linear scaling is achieved for HDG, albeit at relatively high cost. The transformed system streamlines the operation count of operator and preconditioner so that this quantity is lowered to  $1 \mu\text{s}$ . This holds for both, continuous and discontinuous case, rendering the choice of discretization one of preference rather than one of speed. The other variants are somewhat less efficient with larger timings by a factor of to about 5. Still, continuous and discontinuous discretization behave very similar in these cases as well. The attained hallmark of  $1 \mu\text{s}$  enables high-order solutions to the POISSON equation at costs associated with highly optimized low-order solvers, e.g. HPGMG [11], and achieves a main goal of this paper.

## 5.5 Robustness against increases in the penalty parameter

To investigate the robustness against the penalty parameter  $\tau_e$ , the tests of the last section were repeated varying the penalty parameter from 1, to 25, to 625. Figure 5 depicts the solution error and the required number of iterations. An increase of the penalty parameter leads to a reduction of the solution error. However, the larger penalty parameter takes its toll on the condition of the system. The influence depends on the polynomial degree: For  $p = 2$ , a factor of 1.5 occurs when increasing  $\tau$  by a factor of 25, whereas for  $p = 32$ , the effect is far lower. Incidentally, for  $\tau_e = 625$ , the condition of the system seems to improve when increasing  $p$ , again indicating that the system is dominated by the penalty terms at low polynomial degrees.

## 5.6 Robustness against increases in the number of elements

For a constant polynomial degree  $p = 16$ , the number of elements is now scaled from  $n_e = 2^3$  to  $n_e = 16^3$  in this section. Figure 6 depicts the results. It is evident, that the solvers are not robust against increases in the number of elements, as they exhibit a super-linear increase in runtime with regard to the number of elements. The slope of the runtime is close to the  $n_e^{4/3}$  expected for FEM and finite difference approximations with local pre-

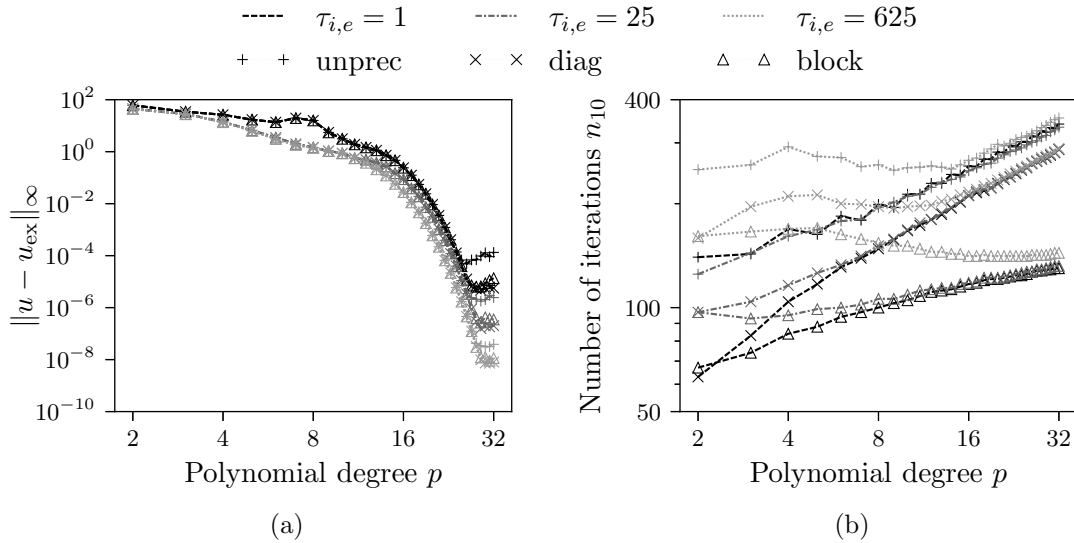


Figure 5: Results when varying the penalty parameter  $\tau_e$  for  $n_e = 8^3$  spectral elements of degree  $p$ . (a): Discretization error. (b): Number iterations required to lower the residual by ten orders.

conditioning [33]. To keep the number of iterations constant, global information transport would be required, for instance with multigrid. In [36], this was facilitated for DG by using overlapping SCHWARZ-type smoothers. These are the most promising candidates for extending the present algorithm towards multigrid, and can be factorized to linear complexity for the continuous discretization, as shown in [24, 17]. However, the derivation of such a factorization for DG requires enough space for a paper of its own.

## 6 Conclusions

This paper considered the residual evaluation for the hybridizable discontinuous GALERKIN method for an elliptic equation. For cuboidal tensor-product elements, the tensor-product decomposition of the operator, in combination with a specific choice of the penalty parameter, and the fast diagonalization technique allowed for a sum factorization. A linearly scaling evaluation method for the HDG operator resulted, i.e. an operation count proportional to  $\mathcal{O}(p^3 n_e) = \mathcal{O}(n_{\text{DOF}})$ . A product factorization lowered the number of operations even further. The linear scaling was, thereafter, validated with runtime tests. In these, the operators were as fast as their counterparts for the static condensed continuous case, and even outperformed them for low polynomial orders.

On this basis, linearly scaling Block-JACOBI type preconditioners were derived from the operator. The combination of linearly scaling operator and preconditioner allowed for conjugate gradient solvers with a completely linearly scaling iteration time. When increasing the polynomial degree, the solvers exhibit only a very slow increase of the number of iterations. In conjunction with an operator that becomes slightly more efficient at higher polynomial degrees, a near constant iteration time per unknown near  $1 \mu\text{s}$  was achieved. Not only was this runtime on par with that attained by the continuous solvers, but it also achieves runtimes usually associated with low-order solvers [11]. Compared to these, the solution is by far more accurate so that the proposed methods constitute a leap forward in terms of error reduction compared to the amount of CPU time invested.

While the solvers proved to scale remarkably well when increasing the polynomial de-

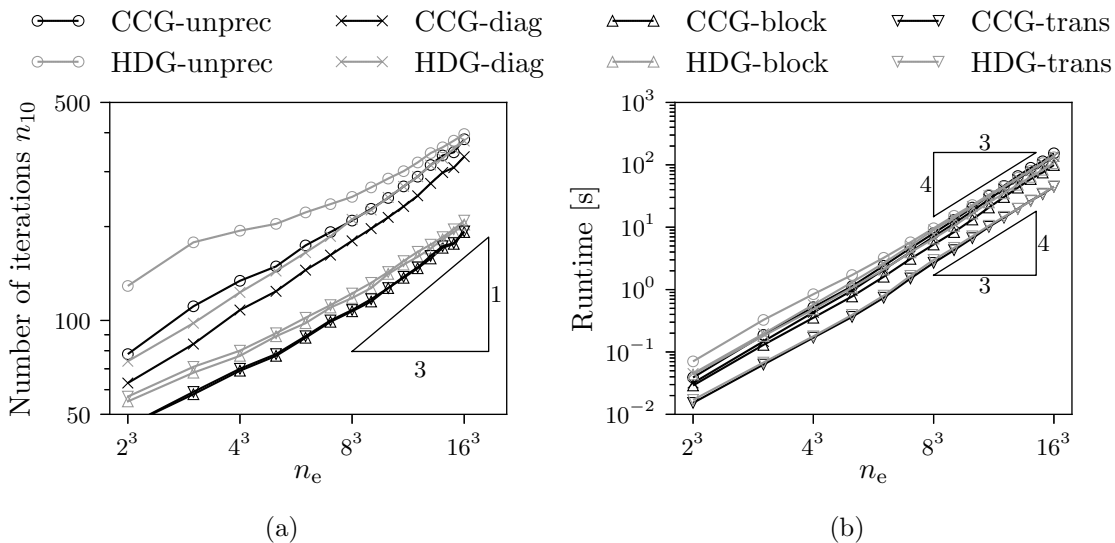


Figure 6: Results when varying the number of elements  $n_e$  in a homogeneous mesh using spectral elements of degree  $p = 16$ . For the HDG solvers, the penalty parameter was fixed at  $\tau_{e,i} = 25$ . (a): Number of iterations required to lower the residual by ten orders. (b): Solver runtimes.

gree, they somewhat lacked robustness against the number of elements. Therefore, the next step will consist of supplementing them with global coupling. Multigrid with overlapping SCHWARZ smoothers is very efficient for both, DG and CG [14, 35, 34]. Moreover, for the static condensed case, the required smoothers were factorized to linear complexity in three dimensions in earlier work [24, 17], which may now be of help. However, it is yet unknown whether the approach extends to the discontinuous case. Iterative substructuring [32], the Cascadic multigrid method [2], or multigrid conjugate gradient methods [31] are further candidates to take into account and were investigated for the continuous method in [19] and [21], respectively. Work in this direction is under way and will be published in a following paper.

### Acknowledgements:

This work is supported in part by the German Research Foundation (DFG) within the Cluster of Excellence ‘Center for Advancing Electronics Dresden’ (cfaed). The authors to thank their colleagues in the Orchestration path of cfaed for stimulating discussions and ZIH, Dresden, for the computational resources provided.

### References

- [1] D. N. Arnold, F. Brezzi, B. Cockburn, and L. D. Marini. Unified analysis of discontinuous Galerkin methods for elliptic problems. *SIAM journal on numerical analysis*, 39(5):1749–1779, 2002.
- [2] F. A. Bornemann and P. Deuffhard. The cascadic multigrid method for elliptic problems. *Numerische Mathematik*, 75(2):135–152, 1996.

- [3] C. Cantwell, S. Sherwin, R. Kirby, and P. Kelly. From h to p efficiently: Strategy selection for operator evaluation on hexahedral and tetrahedral elements. *Computers & Fluids*, 43(1):23–28, 2011.
- [4] P. Castillo, B. Cockburn, I. Perugia, and D. Schötzau. An a priori error analysis of the local discontinuous Galerkin method for elliptic problems. *SIAM Journal on Numerical Analysis*, 38(5):1676–1706, 2000.
- [5] B. Cockburn. Static condensation, hybridization, and the devising of the HDG methods. In *Building bridges: connections and challenges in modern approaches to numerical partial differential equations*, pages 129–177. Springer, 2016.
- [6] B. Cockburn, J. Gopalakrishnan, and R. Lazarov. Unified hybridization of discontinuous Galerkin, mixed, and continuous Galerkin methods for second order elliptic problems. *SIAM Journal on Numerical Analysis*, 47(2):1319–1365, 2009.
- [7] B. Cockburn and C.-W. Shu. The Runge-Kutta local projection  $p^1$ -discontinuous-Galerkin finite element method for scalar conservation laws. *ESAIM: Mathematical Modelling and Numerical Analysis*, 25(3):337–361, 1991.
- [8] M. Deville, P. Fischer, and E. Mund. *High-Order Methods for Incompressible Fluid Flow*. Cambridge University Press, 2002.
- [9] N. Fehn, W. A. Wall, and M. Kronbichler. Efficiency of high-performance discontinuous Galerkin spectral element methods for under-resolved turbulent incompressible flows. *International Journal for Numerical Methods in Fluids*, 2018.
- [10] M. J. Gander and S. Hajian. Analysis of Schwarz methods for a hybridizable discontinuous Galerkin discretization. *SIAM Journal on Numerical Analysis*, 53(1):573–597, 2015.
- [11] A. Gholami, D. Malhotra, H. Sundar, and G. Biros. FFT, FMM, or multigrid? A comparative study of state-of-the-art Poisson solvers for uniform and nonuniform grids in the unit cube. *SIAM Journal on Scientific Computing*, 38(3):C280–C306, 2016.
- [12] J.-L. Guermond, P. Mineev, and J. Shen. An overview of projection methods for incompressible flows. *Computer methods in applied mechanics and engineering*, 195(44):6011–6045, 2006.
- [13] D. Hackenberg, R. Schöne, T. Ilsche, D. Molka, J. Schuchart, and R. Geyer. An energy efficiency feature survey of the Intel Haswell processor. In *Parallel Distributed Processing Symposium Workshops (IPDPSW), 2015 IEEE International*, 2015.
- [14] L. Haupt, J. Stiller, and W. E. Nagel. A fast spectral element solver combining static condensation and multigrid techniques. *Journal of Computational Physics*, 255(0):384 – 395, 2013.
- [15] J. S. Hesthaven and T. Warburton. *Nodal discontinuous Galerkin methods: algorithms, analysis, and applications*. Springer Science & Business Media, 2007.
- [16] F. Hindenlang, G. J. Gassner, C. Altmann, A. Beck, M. Staudenmaier, and C.-D. Munz. Explicit discontinuous Galerkin methods for unsteady problems. *Computers & Fluids*, 61:86–93, 2012.



- [17] I. Huismann. *Computational Fluid Dynamics on Wildly Heterogeneous systems*. PhD thesis, Institute of Fluid Mechanics, TU Dresden, Dresden, 2020. Accepted.
- [18] I. Huismann, L. Haupt, J. Stiller, and J. Fröhlich. Sum factorization of the static condensed Helmholtz equation in a three-dimensional spectral element discretization. *PAMM*, 14(1):969–970, 2014.
- [19] I. Huismann, J. Stiller, and J. Fröhlich. Cascadic multigrid in a spectral-element context. *PAMM*, 16(1):841–842, 2016.
- [20] I. Huismann, J. Stiller, and J. Fröhlich. Fast static condensation for the Helmholtz equation in a spectral-element discretization. In *Parallel Processing and Applied Mathematics*, pages 371–380. Springer, 2016.
- [21] I. Huismann, J. Stiller, and J. Fröhlich. Building blocks for a leading edge high-order flow solver. *PAMM*, 17(1), 2017.
- [22] I. Huismann, J. Stiller, and J. Fröhlich. Factorizing the factorization – a spectral-element solver for elliptic equations with linear operation count. *Journal of Computational Physics*, 346:437–448, oct 2017.
- [23] I. Huismann, J. Stiller, and J. Fröhlich. Efficient high-order spectral element discretizations for building block operators of CFD. *Computers & Fluids*, page 104386, 2019.
- [24] I. Huismann, J. Stiller, and J. Fröhlich. Scaling to the stars—a linearly scaling elliptic solver for  $p$ -multigrid. *Journal of Computational Physics*, 398:108868, 2019.
- [25] P. Jamet. Galerkin-type approximations which are discontinuous in time for parabolic equations in a variable domain. *SIAM Journal on Numerical Analysis*, 15(5):912–928, 1978.
- [26] G. Karniadakis and S. Sherwin. *Spectral/hp Element Methods for CFD*. Oxford University Press, 1999.
- [27] G. E. Karniadakis, M. Israeli, and S. A. Orszag. High-order splitting methods for the incompressible Navier-Stokes equations. *Journal of Computational Physics*, 97(2):414–443, 1991.
- [28] R. M. Kirby, S. J. Sherwin, and B. Cockburn. To CG or to HDG: a comparative study. *Journal of Scientific Computing*, 51(1):183–212, 2012.
- [29] M. Kronbichler and K. Kormann. Fast matrix-free evaluation of discontinuous Galerkin finite element operators. *ACM Transactions on Mathematical Software (TOMS)*, 45(3):29, 2019.
- [30] R. Lynch, J. Rice, and D. Thomas. Direct solution of partial difference equations by tensor product methods. *Numerische Mathematik*, 6(1):185–199, 1964.
- [31] C. Pflaum. A multigrid conjugate gradient method. *Applied Numerical Mathematics*, 58(12):1803–1817, DEC 2008.
- [32] S. J. Sherwin and M. Casarin. Low-energy basis preconditioning for elliptic substructured solvers based on unstructured spectral/hp element discretization. *Journal of Computational Physics*, 171(1):394–417, 2001.

- [33] J. R. Shewchuk. An introduction to the conjugate gradient method without the agonizing pain. Technical report, Pittsburgh, PA, USA, 1994.
- [34] J. Stiller. Robust multigrid for high-order discontinuous Galerkin methods: A fast Poisson solver suitable for high-aspect ratio Cartesian grids. *Journal of Computational Physics*, 327:317–336, 2016.
- [35] J. Stiller. Nonuniformly weighted Schwarz smoothers for spectral element multigrid. *Journal of Scientific Computing*, 72(1):81–96, 2017.
- [36] J. Stiller. Robust multigrid for Cartesian interior penalty DG formulations of the Poisson equation in 3D. In *Spectral and High Order Methods for Partial Differential Equations ICOSAHOM 2016*, pages 189–201. Springer, 2017.
- [37] S. Williams, A. Waterman, and D. Patterson. Roofline: An insightful visual performance model for multicore architectures. *Communications of the ACM*, 52(4):65–76, 2009.
- [38] S. Yakovlev, D. Moxey, R. Kirby, and S. Sherwin. To CG or to HDG: A comparative study in 3D. *Journal of Scientific Computing*, pages 1–29, 2015.